

Kepler Object of Interest Network

II. Photodynamical modelling of Kepler-9 over 8 years of transit observations

J. Freudenthal^{1*}, C. von Essen^{2,1}, S. Dreizler¹, S. Wedemeyer^{3,4}, E. Agol^{5,6,7,8}, B. M. Morris⁵, A. C. Becker⁵,
M. Mallonn⁹, S. Hoyer^{10,11,12}, A. Ofir^{1,13}, L. Tal-Or^{1,14}, H. J. Deeg^{10,11}, E. Herrero^{15,16}, I. Ribas^{15,16},
S. Khalafinejad^{17,18}, J. Hernández¹⁹, and M. M. Rodríguez S.¹⁹

¹ Institut für Astrophysik, Georg-August-Universität Göttingen, Friedrich-Hund-Platz 1, 37077 Göttingen, Germany

² Stellar Astrophysics Centre, Aarhus University, Ny Munkegade 120, 8000 Aarhus, Denmark

³ Rosseland Centre for Solar Physics, University of Oslo, P.O. Box 1029 Blindern, N-0315 Oslo, Norway

⁴ Institute of Theoretical Astrophysics, University of Oslo, P.O. Box 1029 Blindern, N-0315 Oslo, Norway

⁵ Astronomy Department, University of Washington, Seattle, WA 98195, United States of America

⁶ Institut d'Astrophysique de Paris, 98 bis Boulevard Arago, Paris 75014, France

⁷ Guggenheim Fellow

⁸ Virtual Planetary Laboratory

⁹ Leibniz-Institut für Astrophysik Potsdam, An der Sternwarte 16, D-14482 Potsdam, Germany

¹⁰ Instituto de Astrofísica de Canarias, C. Vía Láctea S/N, E-38205 La Laguna, Tenerife, Spain

¹¹ Universidad de La Laguna, Dept. de Astrofísica, E-38206 La Laguna, Tenerife, Spain

¹² Aix Marseille Univ, CNRS, LAM, Laboratoire d'Astrophysique de Marseille, Marseille, France

¹³ Department of Earth and Planetary Sciences, Weizmann Institute of Science, Rehovot, 76100, Israel

¹⁴ School of Geosciences, Raymond and Beverly Sackler Faculty of Exact Sciences, Tel Aviv University, Tel Aviv, 6997801, Israel

¹⁵ Institut de Ciències de l'Espai (IEEC-CSIC), C/Can Magrans, s/n, Campus UAB, 08193 Bellaterra, Spain

¹⁶ Institut d'Estudis Espacials de Catalunya (IEEC), C/Gran Capità 2-4, Edif. Nexus, 08034 Barcelona, Spain

¹⁷ Hamburg Observatory, Hamburg University, Gojenbergsweg 112, 21029 Hamburg, Germany

¹⁸ Max Planck Institute for Astronomy, Königstuhl 17, 69117 Heidelberg, Germany

¹⁹ Instituto de Astronomía, UNAM, Campus Ensenada, Carretera Tijuana-Ensenada km 103, 22860 Ensenada, B.C. México

Received 16/05/2018 / Accepted 28/06/2018

ABSTRACT

Context. The *Kepler* Object of Interest Network (KOINet) is a multi-site network of telescopes around the globe organised to follow up transiting planet candidate KOIs with large transit timing variations (TTVs). Its main goal is to complete their TTV curves, as the *Kepler* telescope no longer observes the original *Kepler* field.

Aims. Combining *Kepler* and new ground-based transit data we improve the modelling of these systems. To this end, we have developed a photodynamical model, and we demonstrate its performance using the Kepler-9 system as an example.

Methods. Our comprehensive analysis combines the numerical integration of the system's dynamics over the time span of the observations along with the transit light curve model. This provides a coherent description of all observations simultaneously. This model is coupled with a Markov chain Monte Carlo algorithm, allowing the exploration of the model parameter space.

Results. Applied to the Kepler-9 long cadence data, short cadence data and 13 new transit observations collected by KOINet between the years 2014 to 2017, our modelling provides well constrained predictions for the next transits and the system's parameters. We have determined the densities of the planets Kepler-9b and 9c to the very precise values of $\rho_b = 0.439 \pm 0.023 \text{ g cm}^{-3}$ and $\rho_c = 0.322 \pm 0.017 \text{ g cm}^{-3}$. Our analysis reveals that Kepler-9c will stop transiting in about 30 years. This results from strong dynamical interactions between Kepler-9b and 9c, near 2:1 resonance, that leads to a periodic change in inclination.

Conclusions. Over the next 30 years the inclination of Kepler-9c (-9b) will decrease (increase) slowly. This should be measurable by a substantial decrease (increase) in the transit duration, in as soon as a few years' time. Observations that contradict this prediction might indicate the presence of additional objects in this system. If this prediction proves true, this behaviour opens up a unique chance to scan the different latitudes of a star: high latitudes with planet c and low latitudes with planet b.

Key words. Stars: planetary systems - Planets and satellites: dynamical evolution and stability - Methods: data analysis - Techniques: photometric - Planets and satellites: individual: Kepler-9b, Kepler-9c - Stars: fundamental parameters

1. Introduction

One of the outstanding results of the *Kepler* mission (Borucki et al. 2010) is the large number of transiting multi-planet systems. Prior to *Kepler's* launch it was shown that the analysis of the dynamical interaction in multi-planet systems would

be feasible offering an independent mass determination (Holman & Murray 2005; Agol et al. 2005). This was impressively confirmed from the first multi-transiting systems (Holman et al. 2010; Lissauer et al. 2011a) using transit timing variations (TTVs), that is, deviations from strict periodicity in planetary transits, caused by non-Keplerian forces. The first compilation of such systems revealed that multi-planet systems are prefer-

* E-mail: jfreude@astro.physik.uni-goettingen.de

entially found among lower-mass planets (Latham et al. 2011) highlighting the advantages of TTVs over radial velocity measurements. Since *Kepler*, the search for transiting multi-planet systems has seen objects like TRAPPIST-1 (Gillon et al. 2016) with three potential habitable rocky planets, Kepler-80, a resonant chain of five planets, and Kepler-90, the first eight-planet system (Shallue & Vanderburg 2018).

Transiting multi-planet systems close to resonance allow the determination of planetary radii and masses – and hence bulk densities – from transit light curves alone, which has been intensively explored by Lissauer et al. (2011b), Jontof-Hutter et al. (2016), and Hadden & Lithwick (2017). A comparison between the two independent mass determinations, namely using radial velocity and transit timing variations, allows for the investigation of systematics due to observational and methodological biases (Mills & Mazeh 2017).

In order to tap the dynamical information of TTVs it is important to cover a full cycle of orbital momentum and energy exchange between the planets (henceforth interaction cycle), which can be substantially longer than their orbital periods. One of the first lists of systems showing TTVs (Mazeh et al. 2013) evidenced the large existing fraction of KOIs that could not be used for dynamical analysis due to long interaction cycles. These were longer than, or of the order of, *Kepler*’s total observing time. This motivated us to create and coordinate the *Kepler* Object of Interest Network, (KOINet¹ von Essen et al. 2018), a network of ground-based telescopes organised to follow up KOIs with large amplitude TTVs. The main goal of KOINet is to coordinate already existing telescopes to characterise the masses of planets and planetary candidates by analysing their observed transit timing variations.

Among the KOINet targets, Kepler-9 is a benchmark system. The star is a solar analog and two of its planets are close to a 2:1 mean motion resonance, with TTV amplitudes of the order of one day. Their deep transits ($\sim 0.5\%$) combined with their large interaction times and the magnitude of the host star ($K_p = 13.803$), make this system ideal for photometric ground-based follow-up.

The first TTV analysis of the Kepler-9b/c system with an incomplete coverage of the interaction cycle had to be complemented with (a few) radial velocity measurements (Holman et al. 2010) which resulted in Saturn-mass planets. The composition of these two planets was investigated by Havel et al. (2011) from evolutionary models, as well as the stellar mass and radius. Using most or all long-cadence *Kepler* data, several authors revised the planetary masses from TTVs alone (Borsato et al. 2014; Dreizler & Ofir 2014) finding masses about half of the values previously reported in the first paper. Dreizler & Ofir (2014) thereby showed that the confirmed innermost planet, Kepler-9d, is dynamically independent from this near-resonant pair. Recently, a new transit observation for Kepler-9b (Wang et al. 2018b) was used to correct its transit time predictions. Additionally, the observation of the Rossiter–McLaughlin effect in radial velocity measurements of Kepler-9 (Wang et al. 2018a) indicates that the stellar spin axis is very likely aligned with the planetary orbital plane.

In this paper we exploit the large amount of short-cadence *Kepler* data, complemented by long-cadence *Kepler* data where short-cadence observations are missing, and extended three years in time by adding corresponding ground-based light curves from KOINet, all wrapped in a detailed photodynamical analysis. The observation of the full interaction cycle by the KOINet

follow-up, together with the comprehensive analysis, results in Kepler-9b and 9c being the system with the highest precision planetary mass and radius determinations. We also constrain the stellar parameters of the host star and predict the dynamical evolution of the system for the next decades.

This paper is divided as follows. We describe the new transit observations by the KOINet, their reduction and analysis in Sect. 2. The structure of the photodynamical model used to analyse KOINet systems is described in Sect. 3. A description of the results from this analysis for the Kepler-9 system can be found in Sect. 4. These results are discussed in Sect. 5. We end this paper with some conclusions in Sect. 6.

2. Observations, data reduction and analysis

Between June, 2014 and September 2017 we observed 13 primary transits of the Kepler-9b/c planets. The photometric follow-up was carried out in the framework of KOINet (von Essen et al. 2018). In this work, we combine the *Kepler* photometry with new, ground-based data which have been collected after the nominal time of the *Kepler* Space Telescope. This section covers the treatment of the new ground-based observations. The photodynamical model described in Sect. 3 was previously fitted to the available *Kepler* data with the aim of getting initial parameters for the ground-based data analysis. A description of the photodynamical analysis on the different data sets follows in Sect. 4.

2.1. Data acquisition and main characteristics of the collected photometry

Table 1 shows the main characteristics of the data presented in this work. These are: the date in which the observations were performed, in years, months and days; the planet observed during transit; an acronym for the telescope used to carry out the observations; the precision of the data in parts-per-thousand (ppt); the number of frames collected during the night, N ; the cadence of the data accounting for readout time in seconds, CAD; the total duration of the observations in hours, T_{tot} ; and the transit coverage, TC. To increase the photometric precision of the collected data, when possible we slightly defocused the telescopes (Kjeldsen & Frandsen 1992; Southworth et al. 2009).

A brief description of the main characteristics of the telescopes involved in this work follows:

- The Oskar Lühning Telescope (OLT 1.2m) has a collecting area of 1.2 meters and is located at the Hamburger Observatory in Hamburg, Germany. The telescope can be used remotely and has a guiding system, minimising systematics caused by poor tracking. Although the seeing at the observatory is rather poor (typical values are around 3–4 arcseconds) it stays constant during the night, allowing photometric precision in the part-per-thousand level. Here we analyse one light curve taken during our first observing season.
- The Apache Point Observatory hosts the Astrophysical Research Consortium 3.5 meter telescope (henceforth ARC 3.5m), and it is located in New Mexico, United States of America. Due to the large collecting area, with this telescope we collected typically 2000 observations per observing run. For our observations, the telescope was slightly defocused. The photodynamical analysis of Kepler-9 presented here includes three light curves taken with the ARC 3.5m during our second observing campaign, in 2015.
- The Wise Observatory hosts a 1 meter telescope that is operated by Tel Aviv University, Israel (WISE 1m). Here we

¹ koinet.astro.physik.uni-goettingen.de

Table 1. Characteristics of the collected ground-based transit light curves of Kepler-9b/c, collected in the framework of KOINet.

| Date yyyy.mm.dd | Planet | Telescope | σ_{res} [ppt] | N | CAD [sec] | T_{tot} [hours] | TC |
|--------------------|--------|-----------|--------------------------------|------|------------------------|-----------------------------|-----------|
| 2014.06.30 | c | OLT 1.2m | 3.6 | 103 | 79 | 2.3 | - - - E O |
| 2015.06.17 | b | ARC 3.5m | 1.9 | 2075 | 8 | 4.7 | O I B - - |
| 2015.07.25 | b | WISE 1m | 2.2 | 132 | 166 | 6.1 | O I B E - |
| | b | CAHA 2.2m | 1.6 | 462 | 57 | 7.4 | O I B E O |
| | b | LIV 2m | 1.2 | 545 | 46 | 7.1 | - - B E O |
| | b | NOT 2.5m | 1.5 | 630 | 28 | 5.0 | - - B E O |
| 2015.08.14 | b | ARC 3.5m | 2.7 | 2095 | 7 | 3.8 | - I B E - |
| 2015.09.01 | c | ARC 3.5m | 2.2 | 2073 | 4 | 2.5 | - - B E O |
| 2015.10.10 | b | IAC 0.8m | 0.5 | 60 | 197 | 3.3 | - I B - - |
| | b | TJO 0.8m | 1.8 | 133 | 61 | 2.3 | - I B - - |
| 2017.05.17 | c | NOT 2.5m | 0.8 | 219 | 79 | 4.9 | O I B E - |
| 2017.06.16 | b | NOT 2.5m | 1.1 | 624 | 30 | 5.4 | - I B E O |
| 2017.06.25 | c | NOT 2.5m | 1.2 | 416 | 42 | 4.9 | O I B - - |
| 2014.06.27 | | OANLH 1m | | | technical difficulties | | |
| 2014.07.23 | | OLT 1.2m | | | technical difficulties | | |
| 2014.08.12 | | OLT 1.2m | | | weather problems | | |
| | | LIV 2m | | | weather problems | | |
| 2015.03.13 | | OLT 1.2m | | | weather problems | | |
| 2016.05.10 | | ARC 3.5m | | | technical difficulties | | |
| 2017.09.01 | | NOT 2.5m | | | weather problems | | |

Notes. The letter code to specify the transit coverage during each observation is the following: O: out of transit, before ingress. I: ingress. B: flat bottom. E: egress. O: out of transit, after egress.

present one transit taken during the second campaign, in 2015.

- The Centro Astronómico Hispano-Alemán hosts, among others, a 2.2 meter telescope (henceforth, CAHA 2.2m). Here we present one complete transit observation of Kepler-9b.
- The 2 meter Liverpool telescope (LIV 2m, [Steele et al. 2004](#)) is located at the Observatorio Roque de los Muchachos, it is fully robotic and is owned and operated by Liverpool John Moores University. In this work we present one transit observation taken with LIV 2m during our second observing season.
- The Nordic Optical Telescope (NOT 2.5m) is located at the Observatorio Roque de los Muchachos in La Palma, Spain. Currently, telescope time for KOINet is assigned via a large (3 year) program. Here, we analyse four light curves taken between the first and fourth observing seasons.
- The 80 centimetre telescope of the Instituto de Astrofísica de Canarias (IAC 0.8m) is located at the Observatorio del Teide, in the Canary Islands, Spain. Observations were collected by KOINet’s observers on site. Here we present one light curve taken during our second observing season.
- The Telescopi Joan Oró (TJO) is a fully robotic 80 centimetre telescope located at the Observatori Astronòmic del Montsec, north-east of Spain (henceforth TJO 0.8m). Here we present one transit light curve.
- The Observatorio Astronómico Nacional Llano del Hato, Venezuela, hosts a 1 meter Zeiss reflector (henceforth OANLH 1m). During scheduled observations, the telescope suffered from technical difficulties.

2.2. Data reduction and preparation

To reduce the impact of our Earth’s atmosphere and the associated telluric contamination in the I-band, and the absorption of stellar light in shorter wavelengths, all of our observations

are carried out using an R-band filter. Observers always provide a set of calibration frames (bias and flat fields) that are used to carry out the photometric data reduction. To reduce the data and construct the photometric light curves we use our own IRAF and python-based pipelines called *Differential Photometry Pipelines for Optimum light curves*, DIP²OL. A full description of DIP²OL can be found in [von Essen et al. \(2018\)](#). In brief, the IRAF component of DIP²OL measures fluxes for different reference stars, apertures and sky rings; the latter two are set in proportion to the intra-night averaged full width at half maximum. The python counterpart of DIP²OL finds the optimum combination of reference stars, aperture, and width of the sky ring that minimises the scatter of the photometric light curves. Once the light curves are constructed, we transform the time stamps from Universal Time to Barycentric Julian Dates in Barycentric Dynamical Time (BJD_{TDB}) using [Eastman et al. \(2010\)](#)’s web tool, all wrapped up in a python script.

To detrend the light curves we compute from the photometric science frames the time-dependent x and y centroid positions of all the stars, the background counts from the sky rings, the integrated flat counts for the final aperture centered around the centroid positions, the airmass and the seeing. A full description of our detrending strategy, how we combine these quantities to construct the detrending function, and the extra care in the particular choice and number of detrending parameters can be found in Sect. 4.2 of [von Essen et al. \(2018\)](#). The detrending components, and the time, flux and errors, are injected into the transit fitting routine.

2.3. First data analysis

Before fitting the full data set using our photodynamical code (see Sect. 3) we carry out a transit fit to each ground-based light curve individually. The main goal of this step is to provide accurate error bars for the flux measurements, that are enlarged to

account for correlated noise (see e.g., [Carter & Winn 2009](#)). A detailed description of the transit fitting procedure can be found in Sect. 4 of [von Essen et al. \(2018\)](#). In brief, once the detrending components are selected, we fit each transit light curve individually. For this we use a detrending times transit ([Mandel & Agol 2002](#)) model, with a quadratic limb-darkening law and thus, quadratic limb-darkening coefficients. The latter are computed as described in [von Essen et al. \(2013\)](#), for stellar parameters closely matching the ones of Kepler-9 ([Holman et al. 2010](#)) and a Johnson-Cousins R filter transmission response. As initial values for all the transit parameters, we use the ones given by the photodynamical analysis carried out on *Kepler* data only. Since the TTVs in this system are so large, all of the transit parameters have to be computed for each specific light curve. When fitting for the transit parameters, rather than using uniform distributions for these parameters, we use Gaussian priors with mean and standard deviation equal to the values computed from our initial photodynamical analysis on *Kepler* data. Only when the transit is fully observed do we allow the model to fit for the semi-major axis, the inclination, and the planet-to-star radius ratio, along with the mid-transit time. Otherwise, all of the transit parameters remain fixed and we fit for the mid-transit time only.

To determine reliable errors for the fitted parameters, we compute them from posterior-probability distributions using a Markov chain Monte Carlo (MCMC) approach. At this stage, we iterate 100 000 times per transit, and discard a conservative first 20 %. Once the best-fit parameters are obtained, we compute residual light curves by subtracting from the data our best-fit transit-times-detrending models. From the residuals we compute the β factor as fully described in Sect. 4.2 of [von Essen et al. \(2018\)](#). Here, we average β values computed in time bins of 0.8, 0.9, 1, 1.1, and 1.2 times the duration of ingress. If this averaged β factor is larger than 1, we enlarge the photometric error bars by this value, and we repeat the MCMC fitting in the exact same fashion as previously explained. The *raw* light curves obtained after the second MCMC iteration with their error bars enlarged, along with the number of detrending components per light curve, are the input parameters of the photodynamical analysis. As a consistency check, after the photodynamical analysis is complete we compare the derived detrending coefficients to the ones obtained from individually fitting the light curves.

2.4. Independent check of the timings

The use of KOINet to carry out TTV studies relates observations taken with several telescopes. As a consequence, the timings will be subject to the accuracy of the ground-based observatories, and the success of KOINet will rely on how accurately the many observatories involved in our photometric follow-up know their own times.

In order to investigate this, on the night of July 25, 2015 we observed Kepler-9b using four different telescopes, namely CAHA 2.2m, LIV 2m, WISE 1m, and NOT 2.5m. Only in the case of CAHA 2.2m did we have full transit coverage. After fitting for the transit parameters as previously specified, we obtained in this case the semi-major axis, a/R_S , the inclination, i , the planet-to-star radii ratio, R_P/R_S , and the mid-transit time, T_0 . The derived values, along with their $1-\sigma$ uncertainties, can be found in the top part of Table 2. Within errors all the fitted parameters are consistent with the values predicted by our photodynamical analysis. The bottom part of the same table shows the individual mid-transit times obtained from fitting all the transit parameters for CAHA 2.2m, and fixing all values except the

Table 2. *Top:* Transit parameters obtained fitting one light curve of Kepler-9b observed with CAHA 2.2m on the night of 2015.07.25. From left to right: transit parameter (TP), transit fitted parameter (TFP) along with $1-\sigma$ uncertainties, and value predicted by our photodynamical analysis (PDA) applied at this stage to *Kepler* data only. *Bottom:* Mid-transit times obtained fitting the three remaining incomplete transit light curves. The first column shows the acronym for the telescope, and the second column the timings along with $1-\sigma$ uncertainties.

| TP, CAHA 2.2m | TFP | PDA |
|---------------|-----------------------|----------------------|
| a/R_S | 29.3 ± 0.2 | 29.27 ± 0.1 |
| $i [^\circ]$ | 88.77 ± 0.03 | 88.76 ± 0.2 |
| R_P/R_S | 0.085 ± 0.001 | 0.079 ± 0.003 |
| Telescope | $T_0 \pm 1-\sigma$ | |
| CAHA 2.2m, | 229.4598 ± 0.0008 | 229.4606 ± 0.005 |
| LIV 2m | 229.4629 ± 0.0009 | |
| WISE 1m | 229.4623 ± 0.0026 | |
| NOT 2.5m | 229.4582 ± 0.0018 | |

Notes. T_0 's are given in $\text{BJD}_{\text{TDB}} - 2457000$.

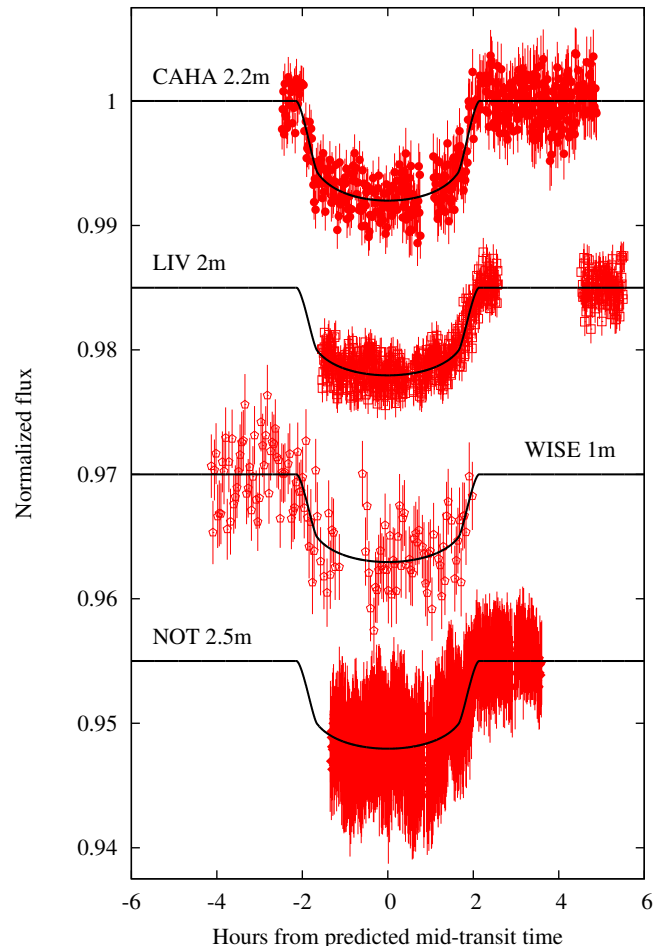


Fig. 1. Detrended transits of Kepler-9b observed on July 25, 2015, by four different telescopes. The transits are artificially shifted for better visual inspection, and plotted as a function of hours from the predicted mid-transit time to appreciate the duration of the observations. Each light curve has been labelled according to the corresponding telescope.

mid-transit times for the remaining three. All mid-transit times are mutually consistent.

Figure 1 shows the quality of our reduction and analysis procedure. From top to bottom, the light curves of Kepler-9b obtained with CAHA 2.2m in filled circles, LIV 2m in empty squares, WISE 1m in empty polygons, and NOT 2.5m in filled diamonds are shown. The light curves have been shifted to the predicted mid-transit time. A visual inspection confirms the equivalency of the derived mid-transit times. The consistency among mid-transit times alleviates the uncertainty that exists when using different sites to follow-up one target.

3. The photodynamical model

With the aim of producing a tool to determine planetary masses that is applicable to all of our KOINet objects, we developed a photodynamical model. Our light curve analysis is based on an n-body simulation of the planetary system over the time span of the observations, combined with a transit light curve model. The numerical integration is implemented in the Mercury6 package by Chambers (1999). We use the second-order mixed-variable symplectic (MVS) algorithm of the package, which is faster than the Bulirsch-Stoer (BS) algorithm but still applicable. The BS integrator would have two advantages, that are the possibility of simulating close encounters and the precision in high frequency terms of the Hamiltonian (discussed by Deck et al. 2014). The former is insignificant as the Kepler-9b/c system does not perform close encounters. The latter was tested to be negligible in our analysis. We calculated the difference of the same TTV model derived with the MVS integrator and the BS algorithm. Within a 50 year integration the difference shows a small slope, that can be corrected by a small change in the mean period smaller than 0.5 s and an oscillation with increasing amplitude. The amplitude of the oscillation is in maximum (in this 50 years) of the order of 55 s which is the order of the precision in the TTVs. For the 8 years of Kepler-9 observations the MVS integrator has a sufficient precision. We added a first order post-Newtonian correction (Kidder 1995) and wrote a python-wrapper for Mercury6 (Husser, priv. comm.). From the n-body simulation we extract the projected distance between planet and star centres, that are in turn used to calculate the transit light curve through the Mandel & Agol (2002) model. Here we use a quadratic limb darkening law already implemented in the occultquad routine. Finally, for each individual planet we correct the output time by the light-travel time effect.

As the numerical integration and its processing is computationally time consuming, we first carry out a coarse integration with a step size equal to only a twentieth of the period of the innermost simulated planet. A more detailed integration is produced for the parts where transits take place and where data are available. For these cases, the detailed integration is done with a step size of 0.01 days, which corresponds to a light curve accuracy of 0.01 ppm for long cadence *Kepler*-data. This accuracy is measured by the mean difference of transit light curves between a model with the given step size and a model with half the step size. For transit light curves, a time step comparable to ingress/egress duration would have a significant impact in the derivation of the transit parameters (Kipping 2010). Therefore, we calculate the transit model on a fine grid (~ 1 minute, when needed) and we rebin it to the actual data points. We describe this in more detail in Sect. 4. For our model calculations, we define the $x - y$ -plane as the plane of the sky, with its origin placed at the stellar centre. Therefore, these coordinates coincide with the projected distances between planet and star mid points. The positive z -axis corresponds to the line of sight, so that the planets transit with positive z -values. The sampling of the Mercury6

integration does not match the observation times. To interpolate the projected distances from the Mercury6 results, we model them with a hyperbola in the range of a transit. The Mandel & Agol (2002) model is calculated for the observation points by these interpolated projected distances, quadratic limb darkening coefficients, and the planet-star radii ratios.

To explore the parameter space, our model is coupled to the Markov chain Monte Carlo emcee algorithm (Foreman-Mackey et al. 2013) accessible in the PyAstronomy² library. All fitting parameters have uniform priors with large limits with the only purpose of avoiding non-physical results. Our choice of free parameters is guided by the modelling rather than by the observations. For instance, Mercury6 uses the semi-major axis, a of the planet as input value. Instead of the period, P , we therefore use a correction factor to a mean semi-major axis a_{adjust} as a free parameter. The mean semi-major axis is calculated through Kepler's third law from the mean period of the transit times of the planets. In addition, the mean anomaly, M , is calculated from this mean period, as well as the reference time, ΔT_0 . As a free parameter we have an addend to this derived mean anomaly M_{adjust} . Furthermore, Mercury6 uses the eccentricity, e and the three angles that describe the position of the orbits on the sky. They are the orbital inclination, i , the argument of the periastron, ω , and the longitude of the ascending node, Ω . As the orientation in the plane of the sky is not directly measurable, Ω is fixed to zero for the innermost simulated planet. In this way, the corresponding values of the other planets show the difference in comparison to this first one. Last but not least, Mercury6 requires the masses, m , of the central star and the planets. These are given by an absolute value for the central star, the ratio of the masses of the innermost simulated planet to the central star, and the ratio of masses of the other planets to the innermost planet.

In order to calculate the transit light curve from the output of Mercury6, the stellar radius, R_s , is required to calculate the relative planet-star distance normalised to the stellar radius. The transit measurements constrain the stellar density (Agol & Fabrycky 2017), but we choose to directly use the required model parameters. Instead of the stellar density we input the stellar mass and radius, but fixing one of them during the modelling. In addition, the occultquad routine requires the planet-star radius ratio, R_p/R_s , and the two quadratic limb darkening coefficients, c_1 and c_2 .

4. Dynamical analysis of Kepler-9

To dynamically characterise the Kepler-9b/c system we carried out three different approaches. Firstly, in order to compare the photodynamical model with the dynamical analysis of only transit times, we fitted our model to quarter 1 through 16 *Kepler* long cadence data (hereafter data set I). This allowed us to compare our results to the ones given by Dreizler & Ofir (2014). Secondly, we attempted to constrain the stellar radius by means of *Kepler* short cadence data, since they have a thirty times higher sampling. Towards this end, we replaced *Kepler* long cadence with short cadence data when available. Specifically for Kepler-9, short cadence data is available between quarter 7 and 17 (data set II). Finally, the model is applied to the full data set, which comprises long cadence data for *Kepler* quarters 1 to 6, short cadence data covering quarters 7 to 17, and all new ground-based light curves, 13 in total, that were collected via the KOINet (data set III).

² <https://github.com/sczesla/PyAstronomy>

The results from all the data analysis and a comparison to previous analysis are listed in Table 3. The top part of the table shows the stellar parameters. The literature values of the stellar radius and density parameters are taken from Havel et al. (2011), and the respective quadratic limb darkening values are taken from the NASA Exoplanet Archive (Mullally et al. 2015). The bottom part of Table 3 shows the derived planetary parameters. They are compared to the results given by Dreizler & Ofir (2014). In this work the authors modelled the transits observed in long cadence data individually, from where the mid-transit times were derived. Afterwards, they dynamically modelled these transit times.

The osculating orbital elements are given at a reference time, BJD = 2454933.0. Fitting the transit times found in Dreizler & Ofir (2014) with a linear time-dependent model we obtained the reference times, $\Delta T_b = 25.26$ d and $\Delta T_c = -3.08$ d as the intercepts, and the mean periods, $P_b = 19.247$ d and $P_c = 38.944$ d as slopes. The reference times and mean periods are used for the determination of the semi major axis and the mean anomaly for all data sets, as described previously in Sect. 2.

During our photodynamical modelling we chose to fix the stellar mass to its literature value, $m_s = 1.05 \pm 0.03 M_\odot$ (Havel et al. 2011). Derived parameters that depend on this value are the planetary masses, as the model parameters are given with respect to the stellar mass. Therefore, the uncertainties of the derived parameters are increased using error propagation including the uncertainty of the stellar mass, $\sigma_{m_s} = 0.03 M_\odot$. When applied, in Table 3 these parameters are labelled with " σ_{m_s} prop.". The calculated densities of the star and the planets depend on the stellar mass in the same way. The semi-major axes are also affected. These are computed from the mean period through Kepler's third law, which also includes the stellar and planetary masses. As a consequence, this error is also propagated into the uncertainty of the semi-major axis.

A quick comparative look at Table 3 shows how the limb darkening coefficients obtained modelling data set I significantly differ from their literature values. We address this issue in Sect. 5. With this exception, within $1\text{-}\sigma$ errors all planetary parameters are in agreement with prior results. The errorbars decrease from modelling data set I to III. The causes of this will be given in detail in the following sections.

4.1. Treatment of the Kepler data

To prepare *Kepler's* transit photometry we first extracted three times the transit duration symmetrically around each transit mid point. To account for intrinsic stellar photometric variability we normalised each transit light curve dividing this by a time-dependent second order polynomial fitted to the out-of-transit data points. To obtain the coefficients of the polynomial functions, we used a simple least squares minimisation routine. As previously mentioned, for long cadence data the light curve model is oversampled by a factor of 30 and rebinned to the actual data points. This procedure is not necessary for short cadence data. The high signal-to-noise ratio of *Kepler* data allowed us to include the quadratic limb darkening coefficients into our model budget.

4.2. Treatment of ground-based data

Due to the lower signal-to-noise ratio of the ground-based data, we fixed the quadratic limb darkening coefficients to values derived from stellar evolution models for the R-band filter, which

we used for all our observations. For stellar parameters closely matching the ones of Kepler-9, the derived limb darkening coefficients are $c_1 = 0.46$ and $c_2 = 0.17$. The best matching coefficients of the detrending components for each ground-based observation, that are derived previously (see Sect. 2.3), are calculated as a linear combination at each call of the photodynamical model.

4.3. Statistical considerations

We performed the analysis of data set I with 36 walkers each, iterating over 30 000 steps. The starting parameters of the walkers are randomly chosen from a normal distribution around the parameter results of Dreizler & Ofir (2014) with a $3\text{-}\sigma$ width. The walkers needed 2 000 iterations to burn in, with the exception of one that finished in a higher χ^2 minimum. Thus, our results are derived from 35 walkers with 28 000 iterations each. We calculated the autocorrelation time for each parameter following Goodman & Weare (2010), but averaging over the autocorrelation function per walker instead of averaging directly over the walker values like discussed in the Blog by Dan Foreman-Mackey³. These calculations results in an autocorrelation time of 1 853 in average (2 771 in maximum), which gives us an effective sample size of 528 (353 in minimum). Each parameter shows a Gaussian posterior distribution from which we extract the median and standard deviation values as best-fit values and errors, respectively. Our results are shown in Table 3. The best-fit solution has a reduced χ^2 of 1.48.

The analysis of data set II is performed using 36 walkers with 20 000 iterations each. In this case, after 4 000 iterations they burned in, with the exception of 2 walkers that ended in a higher χ^2 minimum. The autocorrelation time averages out at 927 (1 648 in maximum), which gives an effective sample size of 586 (330 in minimum). The resulting parameters are derived using the median and standard deviation of the posterior Gaussian distribution. The best solution of this analysis has a reduced χ^2 of 1.06.

The modelling of data set III is accomplished by 36 walkers with 20 000 iterations each. Thirty-five of the walkers burned in after 2 000 iterations. The resulting Gaussian distributions of the 630 000 iterations for the parameters and their correlations can be seen in the appendix in Fig. A.7 for the mass-dependent parameters, in Fig. A.8 for the radius-dependent parameters, and in total in Fig. A.9. Our best-fit solution has a reduced χ^2 of 0.97. The autocorrelation length of this analysis is given by a value of 694 in average (1 105 in maximum). This results in an effective sample size of 907 (570 in minimum).

4.4. Results

The comparison of the best models to the most recent light curves from 2017 displayed in Fig. 2 clearly shows how the inclusion of our new ground-based light curves leads to the improvement of the derived parameters. The top plot shows a Kepler-9b transit light curve in red observed on June 16, 2017. The bottom plot shows a Kepler-9c transit light curve in blue observed on May 17, 2017. Both light curves were obtained using the NOT 2.5m telescope. The variation of 500 randomly chosen good models for data set II are given by the light transparent yellow areas, which can be compared to the corresponding ones obtained including all new ground-based data (data set III). These are plotted in the figures with a light transparent black area. Ad-

³ <http://dfm.io/posts/autocorr>

Table 3. Stellar and planetary parameters derived from the photodynamical modelling of data set I in the second column, data set II in the third column, data set III in the fourth column, along with bibliographic values (Dreizler & Ofir 2014) in the fifth column for comparison. Given are the median and standard deviation values from the MCMC posterior distributions. For the stellar radius and density, the bibliographic values are taken from Havel et al. (2011). The quadratic limb darkening coefficients are taken from Mullally et al. (2015). The sixth column displays some parameters corrected by investigating stellar evolution models in section 5.4. The osculating orbital elements are given at a reference time, BJD = 2454933.0.

| Parameter | Data set I | Data set II | Data set III | Literature | MESA |
|--|-----------------|-----------------|-----------------|-------------|------------------------------|
| Stellar parameters: | | | | | |
| $m_S [M_\odot]$ | 1.05(3) (fixed) | 1.05(3) (fixed) | 1.05(3) (fixed) | 1.05(3) | $1.04^{+0.07}_{-0.04}$ |
| $R_S [R_\odot]$ | 0.947(21) | 0.9755(92) | 0.9742(83) | 1.05(6) | $0.971^{+0.030}_{-0.021}$ |
| $\rho_S^* [\text{g cm}^{-3}]$ | 1.74(12) | 1.596(45) | 1.603(41) | 1.12(27) | |
| $\rho_S^* [\text{g cm}^{-3}] (\sigma_{m_S} \text{ prop.})$ | 1.74(13) | 1.596(64) | 1.603(61) | 1.12(27) | |
| $c_{1, \text{Kepler}}$ | 0.281(53) | 0.361(51) | 0.351(47) | 0.4089 | |
| $c_{2, \text{Kepler}}$ | 0.410(95) | 0.251(78) | 0.269(71) | 0.2623 | |
| Planetary parameters: | | | | | |
| m_b/m_S | 0.0001271(11) | 0.0001271(11) | 0.0001281(11) | 0.000129(2) | |
| m_c/m_b | 0.68911(26) | 0.68846(22) | 0.68849(20) | 0.6875(3) | |
| $m_b^* [M_\oplus]$ | 44.36(44) | 44.51(32) | 44.71(24) | 45.1(15) | |
| $m_c^* [M_\oplus]$ | 30.57(30) | 30.64(22) | 30.79(17) | 31(1) | |
| $m_b^* [M_\oplus] (\sigma_{m_S} \text{ prop.})$ | 44.4(13) | 44.5(13) | 44.7(13) | 45.1(15) | $44.4^{+3.0}_{-1.7}$ |
| $m_c^* [M_\oplus] (\sigma_{m_S} \text{ prop.})$ | 30.57(92) | 30.64(90) | 30.79(90) | 31(1) | $30.5^{+2.1}_{-1.2}$ |
| $a_{b, \text{adjust}} [\text{AU}]$ | 0.9992801(21) | 0.9992811(11) | 0.9992801(11) | - | |
| $a_{c, \text{adjust}} [\text{AU}]$ | 1.0015531(31) | 1.0015521(31) | 1.0015531(21) | - | |
| $a_b^* [\text{AU}]$ | 0.14276083(21) | 0.14276096(16) | 0.14276088(14) | 0.143(1) | |
| $a_c^* [\text{AU}]$ | 0.22889883(83) | 0.22889869(63) | 0.22889876(53) | 0.229(2) | |
| $a_b^* [\text{AU}] (\sigma_{m_S} \text{ prop.})$ | 0.1428(14) | 0.1428(14) | 0.1428(14) | 0.143(1) | $0.1423^{+0.0032}_{-0.0018}$ |
| $a_c^* [\text{AU}] (\sigma_{m_S} \text{ prop.})$ | 0.2289(22) | 0.2289(22) | 0.2289(22) | 0.229(2) | $0.2282^{+0.0051}_{-0.0029}$ |
| e_b | 0.06437(74) | 0.06412(54) | 0.06378(40) | 0.063(1) | |
| e_c | 0.068026(92) | 0.067974(73) | 0.067990(68) | 0.0684(2) | |
| $i_b [^\circ]$ | 89.037(85) | 88.931(33) | 88.936(30) | 87.1(7) | |
| $i_c [^\circ]$ | 89.229(41) | 89.177(17) | 89.180(15) | 87.2(7) | |
| $\omega_b [^\circ]$ | 357.17(33) | 357.10(24) | 356.98(20) | 356.9(5) | |
| $\omega_c [^\circ]$ | 169.29(11) | 169.215(95) | 169.194(73) | 169.3(2) | |
| $M_{b, \text{adjust}} [^\circ]$ | 4.0426(48) | 4.0441(50) | 4.0459(39) | - | |
| $M_{c, \text{adjust}} [^\circ]$ | -3.2629(63) | -3.2654(53) | -3.2648(46) | - | |
| $M_b^* [^\circ]$ | 337.01(41) | 337.12(30) | 337.28(24) | 337.4(6) | |
| $M_c^* [^\circ]$ | 313.489(97) | 313.553(87) | 313.575(67) | 313.5(1) | |
| $\Omega_b [^\circ]$ | 0 (fixed) | 0 (fixed) | 0 (fixed) | 0 (fixed) | |
| $\Omega_c [^\circ]$ | -1.37(15) | -1.244(88) | -1.268(75) | 0(fixed) | |
| R_b/R_S | 0.07644(60) | 0.07766(30) | 0.07759(27) | 0.0825(1) | |
| R_c/R_S | 0.07498(60) | 0.07601(32) | 0.07595(28) | 0.0796(2) | |
| $R_b^* [R_\oplus]$ | 7.91(24) | 8.27(11) | 8.252(94) | 11.1(1) | $8.22^{+0.26}_{-0.18}$ |
| $R_c^* [R_\oplus]$ | 7.76(23) | 8.10(10) | 8.077(92) | 10.7(1) | $8.05^{+0.25}_{-0.18}$ |
| $\rho_b^* [\text{g cm}^{-3}]$ | 0.495(47) | 0.434(17) | 0.439(15) | 0.18(1) | |
| $\rho_c^* [\text{g cm}^{-3}]$ | 0.362(34) | 0.319(12) | 0.322(11) | 0.14(1) | |
| $\rho_b^* [\text{g cm}^{-3}] (\sigma_{m_S} \text{ prop.})$ | 0.495(60) | 0.434(24) | 0.439(23) | 0.18(1) | |
| $\rho_c^* [\text{g cm}^{-3}] (\sigma_{m_S} \text{ prop.})$ | 0.362(44) | 0.319(18) | 0.322(17) | 0.14(1) | |

Notes. * derived, not fitted parameters

ditionally, the difference between the best model of data set II and III can be seen in the bottom panels of the plots (henceforth residual plots). Comparing the yellow and the black areas shows a slight narrowing of the model variation for data set III, which is reflected by the slightly smaller errorbars in Table 3. In the case of Kepler-9b, the transit models slightly shift towards earlier transits when all ground-based data are included. This can be recognised by comparing the yellow and black areas, but it is more obvious in the residual plots. A larger change between modelling the different data sets appears for Kepler-9c. The residuals of the best model for this transit shows an asym-

metric difference between the modelling of data set II and III. That means an adjustment not only in the transit time, but also in the transit shape.

The obtained detrended ground-based transit light curves are shown in Fig. A.1, together with the best photodynamical model in grey, and the variation of 500 randomly chosen good fitting models in black. The data corresponding to Kepler-9b are plotted in red, and the ones of Kepler-9c are plotted in blue. Each observation has its own sub-figure, where the date and the used telescope are indicated. The transits that were observed from dif-

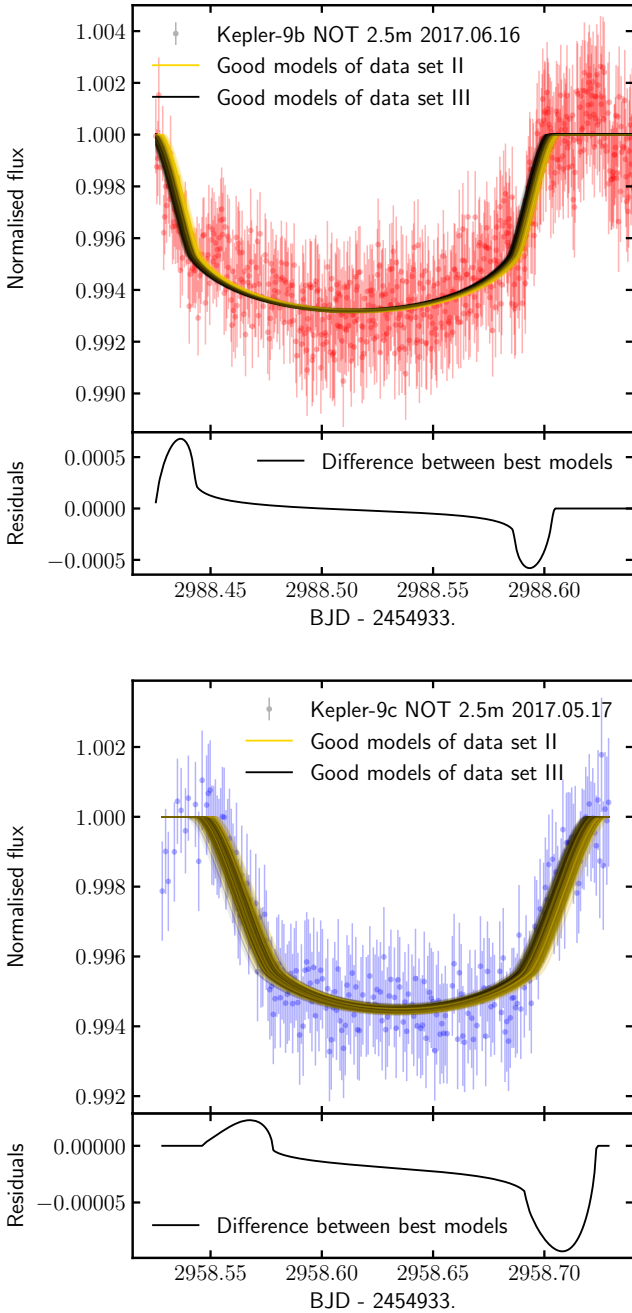


Fig. 2. Examples of new obtained transit light curves for Kepler-9b in red (top), observed on June 16, 2017, and Kepler-9c in blue (bottom), observed on May 17, 2017. Both transits were observed using the NOT 2.5m telescope. Overplotted is the variation of 500 randomly chosen good models by modelling data set II in yellow and modelling of the full data set (data set III) in black. The residuals plot shows the difference between the best models of these two data sets.

ferent sites simultaneously are artificially shifted to allow for a visual inspection. Raw photometry are available for download.

Another derivable parameter of our photodynamical model are the transit times. Figure 3 shows the O-C diagram of the transit times measured by individually fitting the *Kepler* data, as well as the newly obtained ground-based data, in comparison to the results of modelling data set III. Also included is the mid transit time of Kepler-9b obtained by Wang et al. (2018b), about 2σ off from our model and our new data. Unfortunately,

the photometric data are not published so we could not include it in our photodynamical analysis. The top part of Fig. 3 shows the O-C diagram with the transit times from *Kepler* data in orange for Kepler-9b and in light blue for Kepler-9c. The O-C data from the new KOINet observations are shown in red for Kepler-9b and blue for Kepler-9c. The mid-time derived by Wang et al. (2018b) is shown in pink. The transit times from the best photodynamical model of data set III minus the linear trend are presented as grey lines. The middle part of this figure shows the residuals for Kepler-9b with the same colour identification, and the residuals of Kepler-9c are shown respectively in the bottom part. In both residual plots, the 99.74% confidence interval of 1000 randomly chosen good models of the different data sets in comparison to the best model of data set 3 are plotted as grey areas. The light grey area belongs to the modelling of data set I, middle grey to data set II and dark grey to data set III respectively. The differences in the amplitude of the variations of the models compared to the best model are discussed in the next section. In Table A.1 we provide transit time predictions from modelling data set III for the next ten years.

5. Discussion

The results of the photodynamical modelling of Kepler-9b/c require some interpretation. In this section we will first discuss the dynamical stability of the derived system model, followed by a discussion of the transit timing variations along with their prediction for future observations. Furthermore, an emphasis will be given to the transit shape variations and the consequential prediction of disappearing transits for Kepler-9c. Moreover, we will address the stellar activity and, connected to this, we investigate the stellar mass, radius, and age. The age is explored from stellar evolution models as well as gyrochronologically. As the photodynamical modelling yields precise densities, our derived values are also the subject of discussion. Furthermore, the available radial velocity measurements of this system have not been mentioned in this paper; the reasons behind this choice will be addressed here as well. The last point of this section deals with the innermost confirmed planet of the system, that is not included in the analysis. Finally, we discuss the possibility of detect other planets in the system by means of the observed TTVs of Kepler-9b/c.

5.1. Dynamical stability

A dynamical analysis leads naturally to the question of the long term stability of the derived planetary system, as an unstable result should not be considered as a viable model, contradicting the long lifetime of the system. To test the stability of our results for the Kepler-9 system, our best photodynamical solution was extended in time up to 1 Gyr. For this purpose we used the second-order mixed-variable symplectic algorithm implemented in the Mercury6 package by Chambers (1999). This is the same integrator used in our photodynamical model, also including the post-Newtonian correction (Kidder 1995). The time step size we used was 0.9 days, which is slightly smaller than a twentieth of the period of the innermost planet considered in our dynamical analysis, Kepler-9b. This step size gives a good compromise between reasonable computation time and small integration errors. We find that over the integration time the modelled planetary system remains stable. Given the architecture of the system, this was expected, and we can assume that the very similar good results from MCMC modelling should remain stable as well.

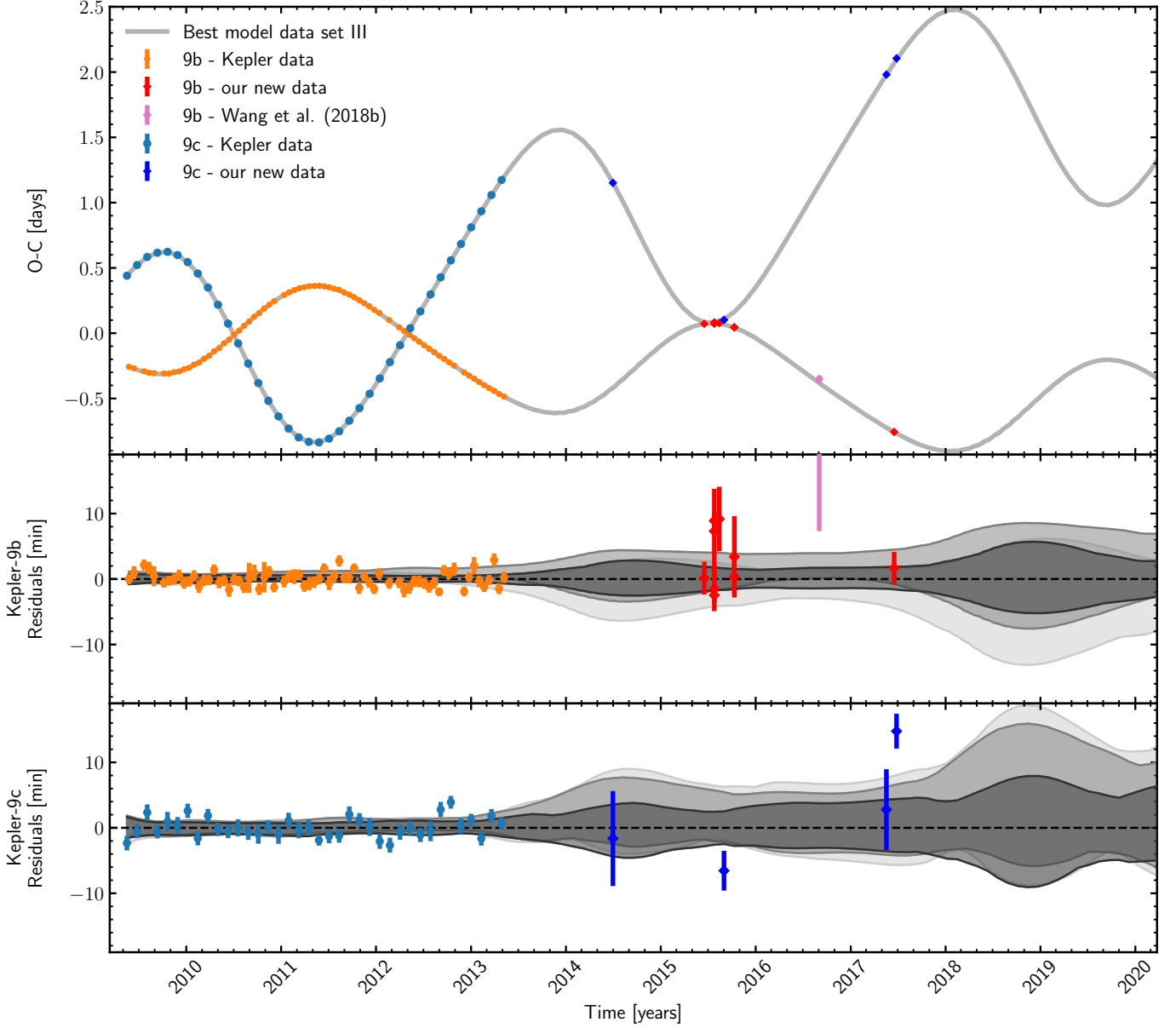


Fig. 3. The O-C diagram of transit times from photodynamical modelling of the data set III and the predictions until 2020 (top). Calculated (C) are transit times from a linear ephemeris modelled at the transit times found by [Dreizler & Ofir \(2014\)](#). The residual plots (middle: Kepler-9b, bottom: Kepler-9c) shows the 99.74% confidence interval of 1000 randomly chosen good models in comparison the best found model of data set 3. From light to dark grey: modelling of data set I, II and III. The *Kepler* transit times are derived by single transit modelling. The new transit time data points originate from the first analysis described in Sect. 2.3.

5.2. Transit timings

After the *Kepler* observations, the variation of good MCMC models in comparison to the best data set III model show different amplitudes as time progresses (see for instance the time range around 2014–2015, and around 2018–2020, Fig. 3). These variations are illustrated by the grey areas in different shades for the modelling of the different data sets, from light to dark grey corresponding to data sets I, II, and III. At the specific times previously mentioned, the variations increase for both planets. This behaviour appears when the O-C has a positive slope for Kepler-9b, and a negative slope for Kepler-9c. At these places the gradient of the TTVs is larger in comparison to the parts where Kepler-9b shows decreasing TTVs and when Kepler-9c shows

increasing TTVs. A larger gradient leads to a larger uncertainty in the predictions. Despite the lower precision in comparison to the space-based *Kepler* data, the new ground-based KOINet observations helped to set tighter constraints on the modulation of the timings. Unfortunately, besides one observation, we missed the chance to observe transits in the phase of higher variation amplitude in 2014. The next time with a higher amplitude starts in 2018, that means another few observations during 2018, especially Kepler-9c transits, will help to tighten the modulation even more.

5.3. The disappearance of Kepler-9c transits

One of the advantages of our photodynamical modelling is the physical consistency in modelling variations in the transit shape due to variations in the transit parameters. These variations can be explained by the dynamical interaction of all objects in the system. Figure 4 shows these variations in the transit shape. Plotted are the transit light curve data per planet shifted by their individual transit time. For a better visualisation of this effect, we plotted only *Kepler* quarter 1 through 17 long cadence data. The higher scatter of short cadence data would lead to a larger range in flux. In turn, the variation of the model would appear diminished due to the larger data range. The model variation is shown in black, which is the best model for each of the transits modelled in data set III, shifted to a common time of transit. For Kepler-9c especially there is a clear variation in the transit shape visible, both in transit depth and transit duration.

The variations in transit shape is not only best visible on long cadence data, but also most significant. The same TTV model with an averaged transit shape model gives a 8% worse reduced χ^2 on data set I. On data set II and III the difference in the reduced χ^2 is only of the order of 0.5%. Nevertheless, photodynamical modelling has the advantage of consistently model the TTVs with the transit shape determining parameters, that is mainly the inclination.

The observed variation in the transit shape of Kepler-9c leads us to examine the evolution of transit parameters over time. Figure 5 shows the variations of the semi-major axis, the eccentricity and the inclination with the predictions for the next 50 years. The predictions for the inclination of Kepler-9c show a continuous decrease, so that both the derived impact parameter b and the transit duration indicate the disappearance of the transits around the year 2052. This behaviour is shown in Fig. 5 as well. A long term inspection reveals the variations in inclination to be a periodic effect, so that the transits will return around 2230 again (see Fig. A.2 in the appendix). Through the decreasing inclination, within the next 35 years we will have the opportunity to map the high latitudes and hence measure the limb of Kepler-9 with frequent transit observations of planet c. In these higher latitudes the transit spends more time at the limb than in the case of a passage of the mid-point of the star. This fact could help in getting more information of the atmospheric structure at the limb.

On the other hand, for planet b an increasing inclination in the next 100 years is predicted (see Fig. A.2 in the appendix). Wang et al. (2018a) measured a stellar spin alignment with the planetary orbital plane on a high probability. As this result might be affected by stellar spot crossings, more Rossiter–McLaughlin measurements are necessary for a confirmation (Oshagh et al. 2016). Nevertheless, assuming spin alignment, Kepler-9b will scan the latitudes between above 30° now down to around 10° . With Kepler-9 being a solar analog, a spot appearance similar to the sun between 0° and 30° is a reasonable assumption. Under those circumstances, measuring spot crossings by Kepler-9b in precise transit observations in the future has a high probability. Such detections would lead to a starspot distribution measurement like in the work of Morris et al. (2017) in which the system analysed, HAT-P-11, is known to be highly misaligned. Hence, an even more similar analysis is possible if the spin alignment of Kepler-9 is not confirmed, in which case there could possibly be spot contamination in the existing transit observations. Spot crossings are not resolvably measured, so a higher accuracy would be necessary for this end.

The existing coverage of latitudes by transit observations is illustrated in Fig. A.3 under the assumption of a stellar spin

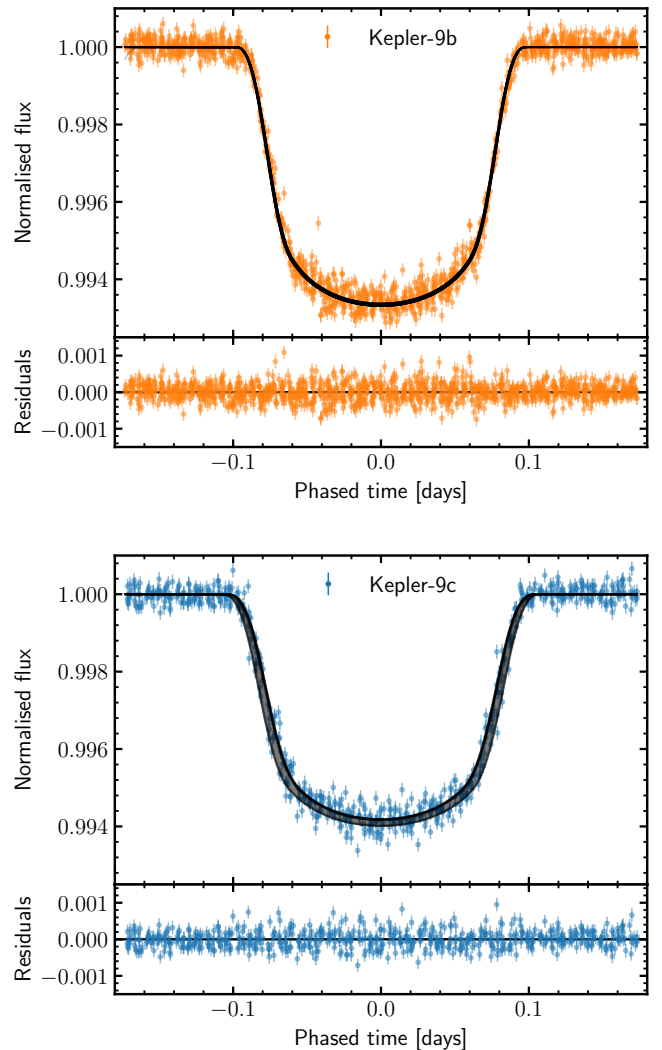


Fig. 4. All long cadence *Kepler* (quarter 1 – 17) data per planet aligned by the transit time in orange for Kepler-9b and in light blue for Kepler-9c. In grey is the best photodynamical model of the full data set, but calculated for only these *Kepler* long cadence data and aligned respectively. The bottom of each figure shows the residuals.

alignment with the orbital plane. The red lines refer to Kepler-9b and blue to Kepler-9c transits. The track is extracted from the best photodynamical model of data set III. The uncertainties in these tracks are retrievable from the impact parameter shown in the fourth row of Fig. 5. The yellow circular disk illustrates the star and the orange area the possible star spot occurrence ranges assuming a similar behaviour to the sun.

The precise *Kepler* data allow us to model the quadratic limb darkening of the star. As a result, from modelling data set III the derived limb darkening coefficients are $c_1 = 0.35 \pm 0.05$ and $c_2 = 0.27 \pm 0.07$. Figure A.8 shows that these two coefficients are highly anti-correlated. This result is consistent with Müller et al. (2013), who investigated the quadratic limb darkening of *Kepler* targets. Additionally, the values suit the literature values given in the NASA Exoplanet Archive (Mullally et al. 2015). The results from modelling data set I demonstrate that using only long cadence *Kepler* data is not sufficient to model the quadratic limb darkening of Kepler-9. Nonetheless, the derived values of $c_1 = 0.28 \pm 0.05$ and $c_2 = 0.41 \pm 0.09$ fit the anti-correlation derived by modelling data set III. This anticorrelation is illustrated

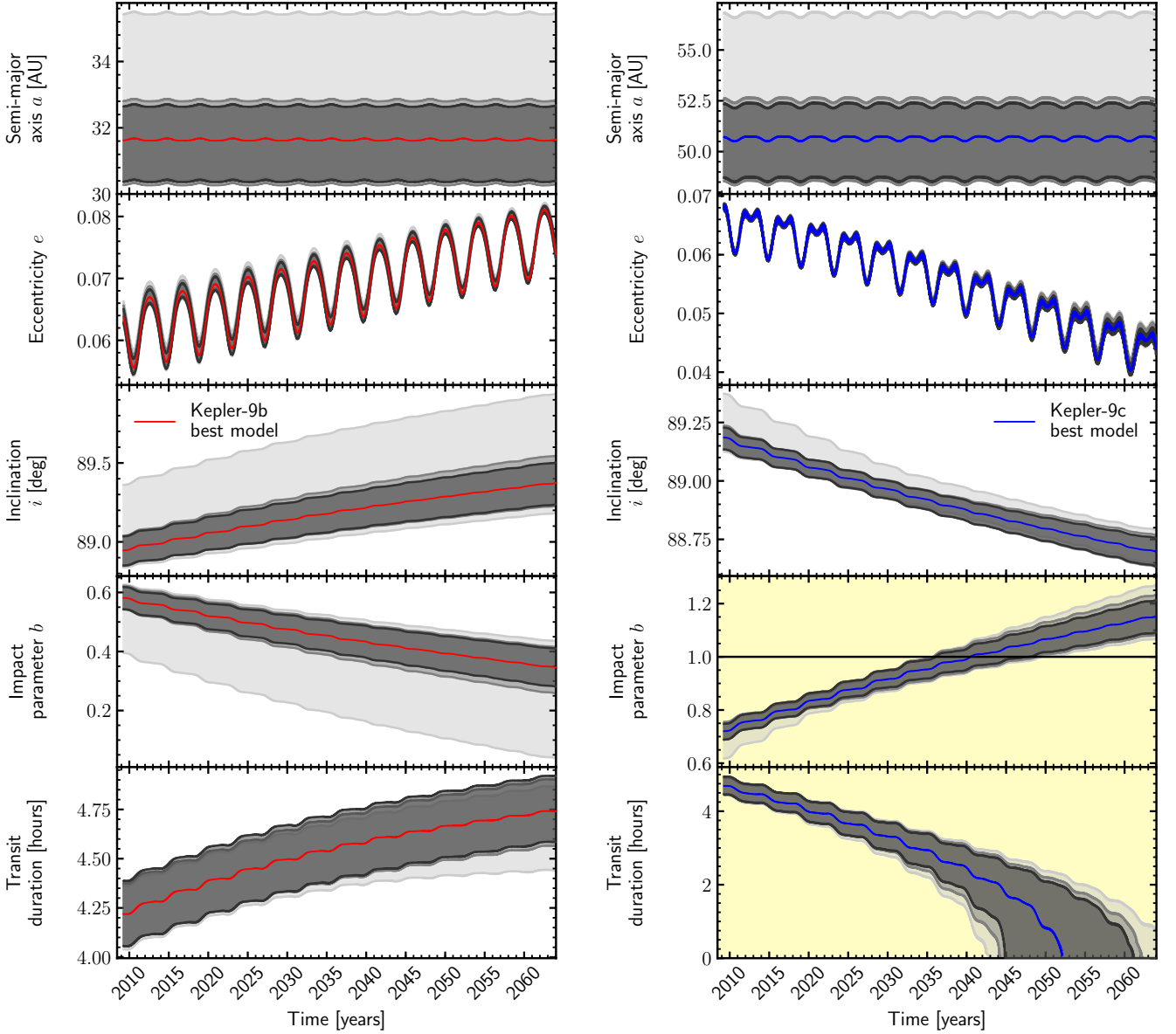


Fig. 5. Top: the extrapolation of the planets semi-major axis until 2065 for the best model in red (Kepler-9b) and in blue (Kepler-9c) and in grey areas the 99.74% confidence interval of 1000 randomly chosen good models for the different data sets. Light grey corresponds to the modelling of data set I, middle grey to data set II and dark grey to data set III respectively. Second: the extrapolation of the planets eccentricity. Third: the extrapolation of the planets inclination. Fourth: the extrapolation of the calculated impact parameter. Fifth: the extrapolation of the calculated transit duration. The background of the impact parameter and the transit duration is coloured for highlighting the place where the prediction of disappearing transits comes from.

in the parameter correlation plot in Fig. A.8. Consequently, the discrepant values lead to different results for the stellar radius and the planet-star radius ratios.

In order to check for model-dependent influences on the resulting evolution of the system parameters, we investigated the differences between Newtonian gravity and the inclusion of a post-Newtonian correction. An analysis was done for the influence on resulting photodynamical models for the Kepler-9b and c. Including the post-Newtonian correction decreased the parameter uncertainties in the second significant figure and the reduced χ^2 in the fifth. The differences are too small to discriminate the models. The future predictions for change in inclination and the transit times behave very similarly.

5.4. On the stellar radius, mass and age

Applying our photodynamical analysis to data set III we determined a stellar density of $\rho_S = 1.603 \pm 0.061 \text{ g cm}^{-3}$. As described in section 3 we modelled the stellar radius instead of the density. However, the transit measurements constrain the stellar density (Agol & Fabrycky 2017). With a fixed stellar mass, the density can be determined straightforwardly. Our modelled density is almost 50% higher than the prior estimate ($\rho_S = (0.79 \pm 0.19) \rho_\odot \hat{=} 1.12 \pm 0.27 \text{ g cm}^{-3}$) by Havel et al. (2011). The authors derived this value from the TTV analysis of the first 3 quarters *Kepler* observations by Holman et al. (2010). With this density, the stellar mass, radius and age was

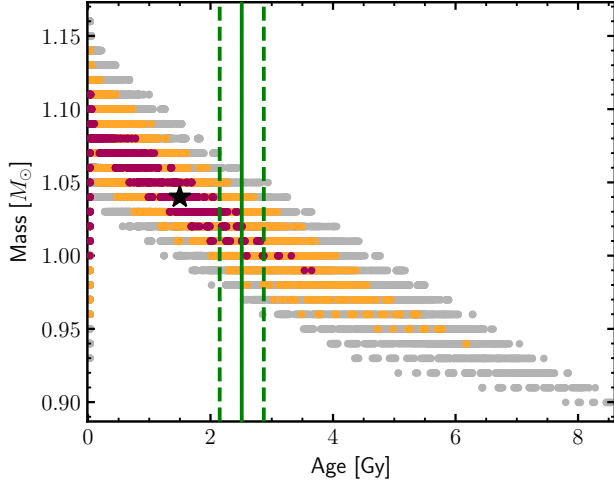


Fig. 6. Mass-age diagram of Kepler-9 from MESA stellar evolution models (MIST). The black star and the red, orange, and grey dots correspond to the best matching value and the 1σ , 2σ , and 3σ areas derived from results on the density of the data set III photodynamical modelling and from new literature values of the effective temperature, the surface gravity, and the metallicity by Petigura et al. (2017). The gyrochronological age is indicated by the green solid line and its 1σ range with the green dashed lines.

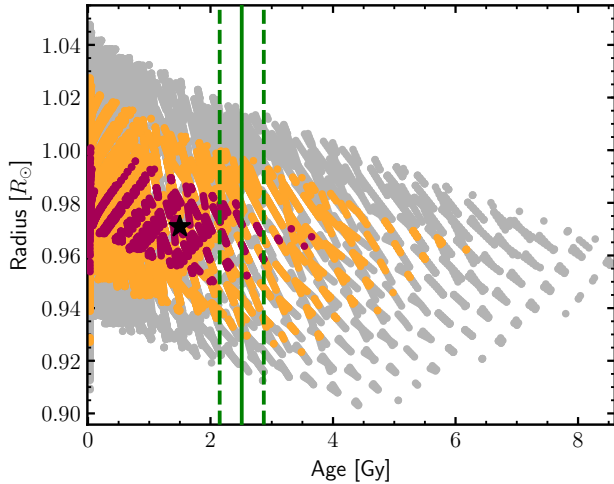


Fig. 7. Radius-age diagram of Kepler-9 from MESA stellar evolution models (MIST). The black star and the red, orange, and grey dots correspond to the best matching value and the 1σ , 2σ , and 3σ areas derived from results on the density of the data set III photodynamical modeling and from new literature values of the effective temperature, the surface gravity, and the metallicity by Petigura et al. (2017). The gyrochronological age is indicated by the green solid line and its 1σ range with the green dashed lines.

determined by stellar evolution models. Our considerably higher derived density motivated a new, similar study of Kepler-9.

We used the stellar density and the known stellar parameters of an effective temperature $T_{\text{eff}} = 5777 \pm 61$ K, surface gravity $\log g = 4.49 \pm 0.09$ and metallicity $\text{Fe}/\text{H} = 0.12 \pm 0.04$ (which classifies Kepler-9 as solar analog, see Holman et al. 2010; Havel et al. 2011) to determine the age, the mass and the radius of the star by stellar evolution models. The results are presented in the

appendix (similar to the below derived Fig. 6 and Fig. 7) in a mass-age diagram in Fig. A.4 and in a radius-age diagram in Fig. A.5. We extracted the corresponding values from the interpolated MESA (Paxton et al. 2011, 2013, 2015) evolutionary tracks by MIST (Dotter 2016; Choi et al. 2016). We derive a stellar mass of $m_S = 1.06^{+0.06}_{-0.05} M_{\odot}$, a radius of $R_S = 0.977^{+0.031}_{-0.024} R_{\odot}$ and an age of $\tau_{\text{Evol}} = 0.95^{+1.88}_{-0.92}$ Gyr.

Recent HIRES observations by Petigura et al. (2017) of more than 1000 KOIs led to the correction of the Kepler-9 stellar parameters to $T_{\text{eff}} = 5787 \pm 60$ K, $\log g = 4.473 \pm 0.1$, and $\text{Fe}/\text{H} = 0.082 \pm 0.04$. Although very similar, the lower metallicity leads to slightly different results. With these new values we determined the stellar mass to $m_S = 1.04^{+0.07}_{-0.05} M_{\odot}$, the radius to $R_S = 0.971^{+0.030}_{-0.021} R_{\odot}$ and the stellar age to $\tau_{\text{Evol}} = 1.49^{+2.15}_{-1.47}$ Gyr. The corresponding diagrams can be found for mass vs. age in Fig. 6 and for radius vs. age in Fig. 7. We like to note that mass and radius for both parameter sets are in agreement within 1σ . The derived age of 1.5 Gyr, however, is in better agreement with the gyrochronological age derived below. With these new values for the stellar mass and radius we corrected the modelled planetary masses, semi-major axes, and radii, which can be found in the sixth column of Table 3.

More recently, the second Gaia data release (Gaia DR2) was carried out (Gaia Collaboration et al. 2016, 2018). The there derived effective temperature of $T_{\text{eff}} = 5750^{+250}_{-130}$ K fits the HIRES value within the 1σ range, so does the stellar radius with $R_S = 0.977^{+0.045}_{-0.080} R_{\odot}$. The values have comparatively higher uncertainties. The distance of Kepler-9 is determined to $p = 1.563 \pm 0.017$ mas by Gaia DR2.

To test the results of the stellar evolution model analysis, we determined the gyrochronological age of Kepler-9. For this, we computed a periodogram of Kepler-9's full long cadence photometry (Lomb 1976; Scargle 1982; Zechmeister & Kürster 2009). The highest power peak corresponds to 16.83 ± 0.08 days. The period and error correspond to the mean and standard deviation obtained fitting a Gaussian to the highest periodogram peak. On Kepler-9, typical photometric variability due to spot rotation has an amplitude of 5 ppt, well above the photometric noise.

To determine Kepler-9's age we made use of Barnes (2007, 2009)'s gyrochronological estimate:

$$\log(\tau_{\text{Gyro}}) = \frac{1}{n} [\log P - \log a - b \times \log(\text{B-V} - c)], \quad (1)$$

for $a = 0.770 \pm 0.014$, $b = 0.553 \pm 0.052$, $c = 0.472 \pm 0.027$, and $n = 0.519 \pm 0.007$. Assuming $\text{B-V} = 0.642$, and following Barnes (2009) error estimates, the derived gyrochronological age for Kepler-9 is 2.51 ± 0.36 Gyr. This age is indicated in the mass-age and radius age diagrams (Fig. 6, Fig. 7, Fig. A.4, Fig. A.5) by green lines, solid for the the median value and dashed for the 1σ range. The gyrochronological age is slightly higher than the age indicated by stellar evolution models, but the values agree within the 1σ range.

5.5. The stellar and planetary densities

In addition to the stellar density, the photodynamical analysis provides strong constraints on the planetary densities. As a result of the analysis performed on data set III we obtained densities of $\rho_b = 0.439 \pm 0.023$ g/cm³ for Kepler-9b and $\rho_c = 0.322 \pm 0.017$ g/cm³ for Kepler-9c. In Fig. 8 our results are compared to literature values from The Extrasolar

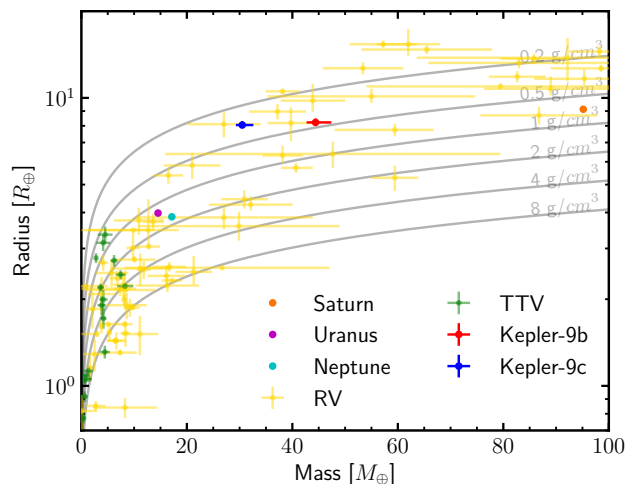


Fig. 8. Mass-Radius diagram for known planets with masses up to $100 M_{\oplus}$. In yellow are the planets with mass measurements obtained by radial velocities and in green the planets with mass measurements obtained from TTVs. The data are given by the *The Extrasolar Planets Encyclopaedia*. Our results are shown in red (Kepler-9b) and in blue (Kepler-9c). For comparison also the values of Saturn, and Uranus and Neptune are shown, the Neptune-like planet pair of our solar system.

Planets Encyclopaedia⁴ for planets with similar properties. Color-coded are the mass measurements obtained from radial velocities in yellow, and from TTVs in green. In this regime, that is the regime of Neptune-like planets, the density measurements of Kepler-9b/c are to date the most precise ones outside the solar system.

To rule out biased results for stellar radius and planet-star radii ratios caused by the photometric variability of Kepler-9, we checked for variability in the residuals of the transit light curves. To be consistent we chose the high-precision, well-sampled *Kepler* short cadence data for this analysis. The scatter of the residuals inside the transit is slightly larger than outside the transit. The standard deviation inside the transit is $\text{std}_{\text{inside}} = 0.001049$, while outside is $\text{std}_{\text{outside}} = 0.001027$ for the best model of data set III. That means 2% difference between inside and outside transit. We did not find any periodicity inside the transit residuals, potentially caused by star spots. Equivalently, the transit time residuals do not show a periodic variability. Nevertheless, the higher scatter inside transit possibly results from unresolved stellar spot crossings. The planet-star radii ratio determination is affected within its uncertainties. With the absence of measurable star spots and the small differences in standard deviation between inside transit and outside, a systematic error in the radius determination seems to be negligible. The planetary densities are therefore also well determined.

Figure 8 shows the similarity of the Kepler-9b/c planets to Saturn in radius. The masses are less than half the value of Saturn, resulting in smaller densities. Their low density implies Kepler-9b/c should be classified as hydrogen-helium gas giants. The formation of the planets happened most likely in the outer region of the system. Through converging migration the planets could be brought in the near 2:1 mean motion resonance in close proximity to the host star (e.g. shown by [Henrard 1982](#); [Borderies & Goldreich 1984](#); [Lemaître 1984](#)). It has been shown

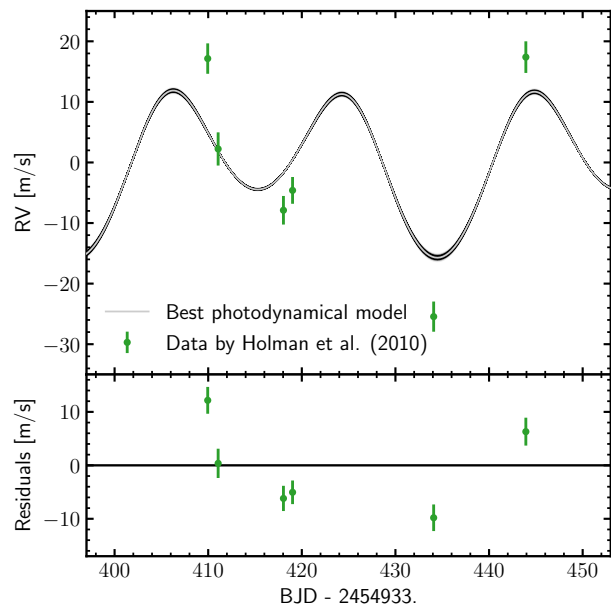


Fig. 9. Results from photodynamical modelling of data set III on the radial velocity measurements by [Holman et al. \(2010\)](#).

that such formation scenarios can result in stable resonant orbits with the outer planet having only about half the mass of the inner one ([Deck & Batygin 2015](#)).

5.6. The radial velocity measurements

In our analysis we did not consider the radial velocity (RV) measurements by [Holman et al. \(2010\)](#) for Kepler-9. The reasons are the small number of measurements, the short time span of the observations, as well as the large discrepancy between a dynamical model to the TTVs and the RV data. Nevertheless, from our photodynamical model we calculated an RV model. Simulated RV models from the results of modelling the full transit dataset are shown together with the data in Fig. 9. The best model has a $\chi^2 = 56.94$ for the 6 RV measurements. As pointed out by [Dreizler & Ofir \(2014\)](#), we also see a similar discrepancy between the dynamical model and these measurements. Additional evidence in favor of the TTV model comes from the short timescale chopping variations seen in planet 9b due to 9c: the amplitude of chopping prefers a smaller mass for planet 9c ([Deck & Agol 2015](#)), which, of course, is included in the full photodynamical constraint.

The most evident reason for this discrepancy is the activity of Kepler-9. A jitter factor would be necessary for including these data in the analysis. A detailed analysis of the activity of the star and the integration of the RV measurements is however beyond the scope of this paper.

In addition, the recently obtained RV measurements listed in the HARPS-N archive⁵, but marked as proprietary could help to constrain the RV behaviour of Kepler-9 better. Figure A.6 shows a prediction of the Kepler-9 radial velocity based on our model constraints for the approximate time span of the new HARPS-N observations.

⁵ <http://archives.ia2.inaf.it/tng/faces/search.xhtml?dsid=9814>

⁴ <http://www.exoplanet.eu/>

5.7. An additional planet?

To complete our analysis we also tested the influence of the third known planet, Kepler-9d (confirmed by [Torres et al. 2011](#)), with a period $P_d = 1.592960(2)$ d on the dynamics of the system. We agree with [Dreizler & Ofir \(2014\)](#) that it does not interact measurably with the two modelled planets, in the plausible mass regime ($m_d = 1\text{--}7 M_\oplus$, [Holman et al. 2010](#)). For a mass of $m_d = 7 M_\oplus$ the reduced χ^2 does not improve and also the variations of the residuals of the transit times are of the same order. The amplitude in radial velocity measurements is of the order of 1 m s^{-1} , far below the precision of the previous observations and currently infeasible for such a faint star as Kepler-9.

Adding another outer planet in a Laplace-resonance (4:2:1) to explain the deviations in the radial velocity measurements would require a rather high mass for the additional planet. Such a planet would have a far too large influence in the system's dynamics and is ruled out by the photodynamical analysis. The fact that only 6 RV measurements are published makes it impossible to set constraints on further possible planets. Additional planets could exist outside the Laplace-resonance that can explain the discrepancies between transit and radial velocity measurements, and yet not influence the short-term dynamics much. In addition there is no periodicity in the transit timing residuals found, that would indicate an outer planet.

6. Conclusions

With this work we substantiated the importance of the KOINet. With its anticorrelated, large amplitude TTVs the Kepler-9b/c system was chosen as benchmark system for the photodynamical modelling. Although the dynamical cycle was almost covered by *Kepler* observations, the 13 new transit observations led to better constraints on the composition of the system. Concurrently, the capability of KOINet to complete a transit observation with long duration by using several telescopes around the globe was confirmed. This is rounded out by the results of the photodynamical modelling. The application to Kepler-9 revealed that the transits of the outer planet will disappear in about 30 years. Furthermore, this dynamical analysis of the combined photometric data, consisting of *Kepler* long and short cadence data, complemented by ground-based follow-up observation, led to the most precise planetary density measurements of planets in the Neptune-mass regime.

From the decreasing inclination of Kepler-9c and increasing inclination of Kepler-9b we have the opportunity to map the different latitudes of the star. Hence, measurements of the limb and possibly star spots of Kepler-9 could be made possible by precise, frequent transit observations within the next 35 years for the limb and 100 years for the star spots. Interspersed with frequent ground-based follow-up, transit measurements from space that provide a high photometric precision would complement the stellar analysis. The promising predictions of this work make Kepler-9 an interesting target for space missions like TESS ([Ricker et al. 2015](#)), PLATO 2.0 ([Rauer et al. 2014](#)) or CHEOPS ([Broeg et al. 2013](#)), though it is a rather faint object with Kepler magnitude of $K_p = 13.803$.

Acknowledgements. We acknowledge funding from the German Research Foundation (DFG) through grant DR 281/30-1. This work made use of PyAstronomy. CvE acknowledges funding for the Stellar Astrophysics Centre, provided by The Danish National Research Foundation (Grant DNRF106). Based on observations made with the Nordic Optical Telescope, operated by the Nordic Optical Telescope Scientific Association at the Observatorio del Roque de los Muchachos, La Palma, Spain, of the Instituto de Astrofísica de Canarias. We acknowledge support from the Research Council of Norway's grant 188910 to finance ser-

vice observing at the NOT. SW acknowledges support for International Team 265 ("Magnetic Activity of M-type Dwarf Stars and the Influence on Habitable Extra-solar Planets") funded by the International Space Science Institute (ISSI) in Bern, Switzerland. EA acknowledges support from United States National Science Foundation grant 1615315. EH and IR acknowledge support by the Spanish Ministry of Economy and Competitiveness (MINECO) and the Fondo Europeo de Desarrollo Regional (FEDER) through grant ESP2016-80435-C2-1-R, as well as the support of the Generalitat de Catalunya/CERCA programme. The Joan Oró Telescope (TJO) of the Montsec Astronomical Observatory (OAdM) is owned by the Generalitat de Catalunya and operated by the Institute for Space Studies of Catalonia (IEEC). Based on observations collected at the Centro Astronómico Hispano Alemán (CAHA) at Calar Alto, operated jointly by the Max-Planck Institut für Astronomie and the Instituto de Astrofísica de Andalucía (CSIC). Based on observations obtained with the Apache Point Observatory 3.5-meter telescope, which is owned and operated by the Astrophysical Research Consortium. The Liverpool Telescope is operated on the island of La Palma by Liverpool John Moores University in the Spanish Observatorio del Roque de los Muchachos of the Instituto de Astrofísica de Canarias with financial support from the UK Science and Technology Facilities Council.

References

- Agol, E. & Fabrycky, D. 2017, ArXiv e-prints [arXiv:1706.09849]
Agol, E., Steffen, J., Sari, R., & Clarkson, W. 2005, MNRAS, 359, 567
Barnes, S. A. 2007, ApJ, 669, 1167–1189
Barnes, S. A. 2009, in IAU Symposium, Vol. 258, The Ages of Stars, ed. E. E. Mamajek, D. R. Soderblom, & R. F. G. Wyse, 345–356
Borner, N. & Goldreich, P. 1984, Celestial Mechanics, 32, 127
Borsato, L., Marzari, F., Nascimbeni, V., et al. 2014, A&A, 571, A38
Borucki, W. J., Koch, D., Basri, G., et al. 2010, Science, 327, 977
Broeg, C., Fortier, A., Ehrenreich, D., et al. 2013, in Hot Planets and Cool Stars, Garching, Germany, Edited by Roberto Saglia; EPJ Web of Conferences, Volume 47, id.03005, Vol. 47
Carter, J. A. & Winn, J. N. 2009, ApJ, 704, 51
Chambers, J. E. 1999, MNRAS, 304, 793
Choi, J., Dotter, A., Conroy, C., et al. 2016, ApJ, 823, 102
Deck, K. M. & Agol, E. 2015, The Astrophysical Journal, 802, 116
Deck, K. M., Agol, E., Holman, M. J., & Nesvorný, D. 2014, ApJ, 787, 132
Deck, K. M. & Batygin, K. 2015, ApJ, 810, 119
Dotter, A. 2016, ApJS, 222, 8
Dreizler, S. & Ofir, A. 2014, ArXiv e-prints [arXiv:1403.1372]
Eastman, J., Siverd, R., & Gaudi, B. S. 2010, PASP, 122, 935
Foreman-Mackey, D., Hogg, D. W., Lang, D., & Goodman, J. 2013, PASP, 125, 306
Gaia Collaboration, Brown, A. G. A., Vallenari, A., et al. 2018, ArXiv e-prints, arXiv:1804.09365
Gaia Collaboration, Prusti, T., de Bruijne, J. H. J., et al. 2016, A&A, 595, A1
Gillon, M., Jehin, E., Lederer, S. M., et al. 2016, Nature, 533, 221
Goodman, J. & Weare, J. 2010, Communications in Applied Mathematics and Computational Science, 5, 65
Hadden, S. & Lithwick, Y. 2017, AJ, 154, 5
Havel, M., Guillot, T., Valencia, D., & Crida, A. 2011, A&A, 531, A3
Henrad, J. 1982, Celestial Mechanics, 27, 3
Holman, M. J., Fabrycky, D. C., Ragozzine, D., et al. 2010, Science, 330, 51
Holman, M. J. & Murray, N. W. 2005, Science, 307, 1288
Jontof-Hutter, D., Ford, E. B., Rowe, J. F., et al. 2016, ApJ, 820, 39
Kidder, L. E. 1995, Phys. Rev. D, 52, 821
Kipping, D. M. 2010, MNRAS, 408, 1758
Kjeldsen, H. & Frandsen, S. 1992, PASP, 104, 413
Latham, D. W., Rowe, J. F., Quinn, S. N., et al. 2011, ApJ, 732, L24
Lemaître, A. 1984, Celestial Mechanics, 34, 329
Lissauer, J. J., Fabrycky, D. C., Ford, E. B., et al. 2011a, Nature, 470, 53
Lissauer, J. J., Ragozzine, D., Fabrycky, D. C., et al. 2011b, ApJS, 197, 8
Lomb, N. R. 1976, Ap&SS, 39, 447
Mandel, K. & Agol, E. 2002, ApJ, 580, L171
Mazeh, T., Nachmani, G., Holczer, T., et al. 2013, ApJS, 208, 16
Mills, S. M. & Mazeh, T. 2017, ApJ, 839, L8
Morris, B. M., Hebb, L., Davenport, J. R. A., Rohn, G., & Hawley, S. L. 2017, ApJ, 846
Mullally, F., Coughlin, J. L., Thompson, S. E., et al. 2015, ApJS, 217, 31
Müller, H. M., Huber, K. F., Czesla, S., Wolter, U., & Schmitt, J. H. M. M. 2013, A&A, 560, A112
Oshagh, M., Dreizler, S., Santos, N. C., Figueira, P., & Reiners, A. 2016, A&A, 593, A25
Paxton, B., Bildsten, L., Dotter, A., et al. 2011, ApJS, 192, 3
Paxton, B., Cantiello, M., Arras, P., et al. 2013, ApJS, 208, 4
Paxton, B., Marchant, P., Schwab, J., et al. 2015, ApJS, 220, 15
Petigura, E. A., Howard, A. W., Marcy, G. W., et al. 2017, AJ, 154

- Rauer, H., Catala, C., Aerts, C., et al. 2014, *Experimental Astronomy*, 38, 249
- Ricker, G. R., Winn, J. N., Vanderspek, R., et al. 2015, *Journal of Astronomical Telescopes, Instruments, and Systems*, 1, 014003
- Scargle, J. D. 1982, *ApJ*, 263, 835
- Shallue, C. J. & Vanderburg, A. 2018, *AJ*, 155, 94
- Southworth, J., Hinse, T. C., Jørgensen, U. G., et al. 2009, *MNRAS*, 396, 1023
- Steele, I. A., Smith, R. J., Rees, P. C., et al. 2004, in *Proc. SPIE*, Vol. 5489, *Ground-based Telescopes*, ed. J. M. Oschmann, Jr., 679–692
- Torres, G., Fressin, F., Batalha, N. M., et al. 2011, *ApJ*, 727, 24
- von Essen, C., Ofir, A., Dreizler, S., et al. 2018, *ArXiv e-prints* [[arXiv:1801.06191](https://arxiv.org/abs/1801.06191)]
- von Essen, C., Schröter, S., Agol, E., & Schmitt, J. H. M. M. 2013, *A&A*, 555, A92
- Wang, S., Addison, B., Fischer, D. A., et al. 2018a, *AJ*, 155, 70
- Wang, S., Wu, D.-H., Addison, B. C., et al. 2018b, *AJ*, 155, 73
- Zechmeister, M. & Kürster, M. 2009, *A&A*, 496, 577

Appendix A: Additional plots and a table of the transit time predictions

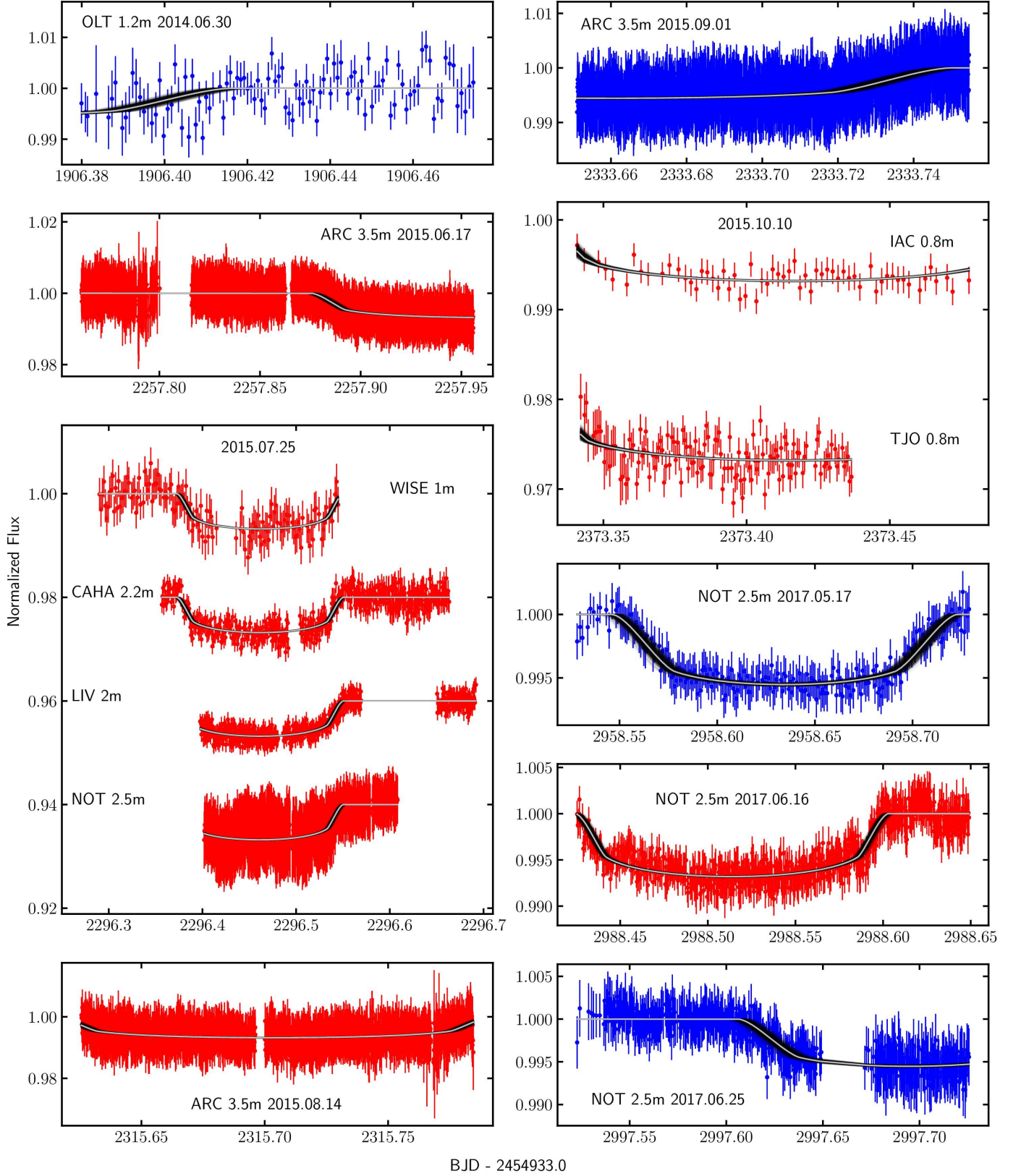


Fig. A.1. Our observed transits with the best data set III model in grey and its variations by 500 randomly chosen good models in black. Transit data in red belong to Kepler-9b and blue transit data correspond to Kepler-9c. The transits of dates with more than one observation are artificially shifted for better visualization and the belonging telescope is indicated.

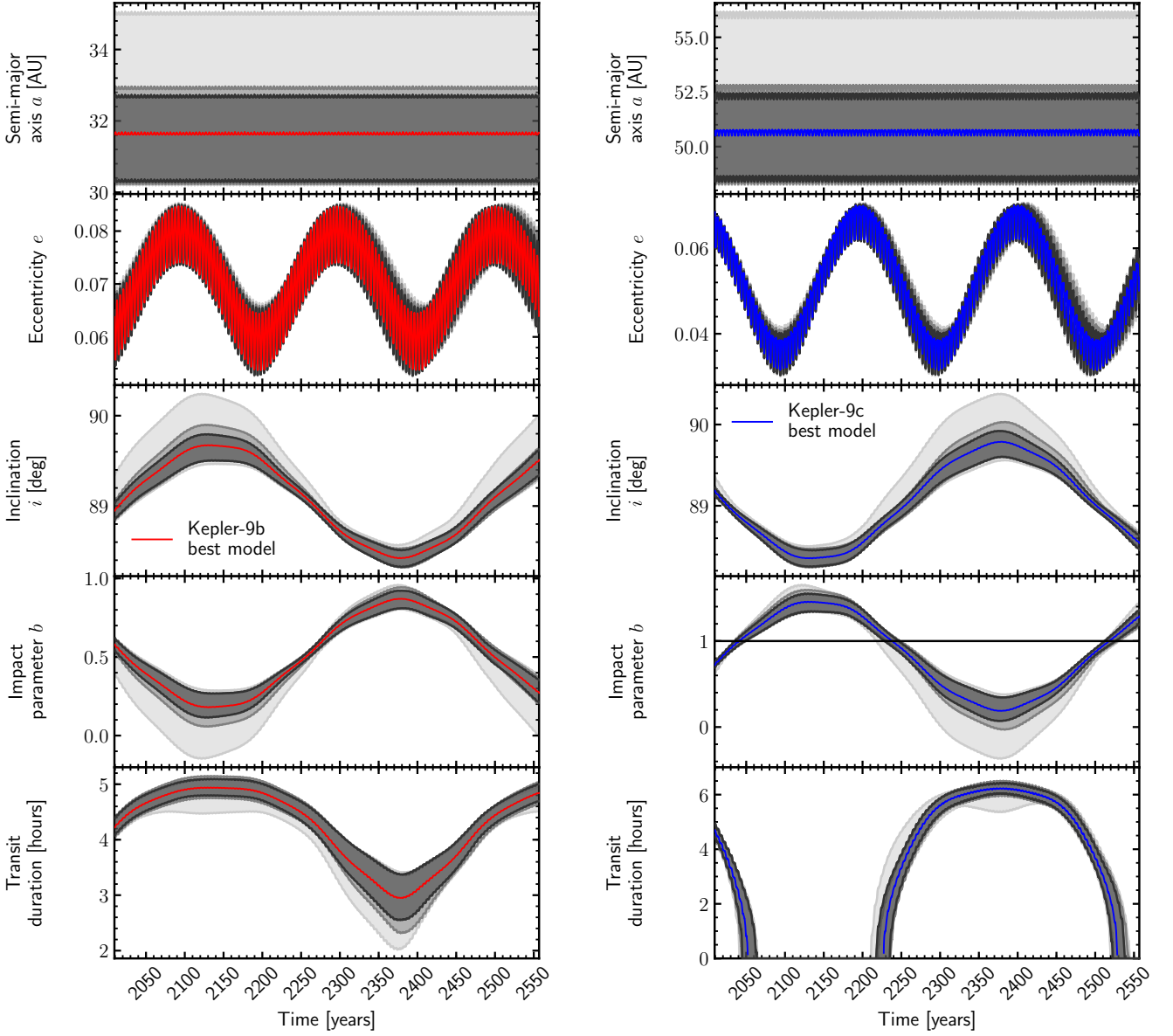


Fig. A.2. Top: the extrapolation of the planets semi-major axis until 2550 for the best model in red (Kepler-9b) and blue (Kepler-9c) and in grey areas the 99.74% confidence interval of 1000 randomly chosen good models for the different data sets. Light grey corresponds to the modelling of data set I, middle grey to data set II and dark grey to data set III respectively. Second: the extrapolation of the planets eccentricity. Third: the extrapolation of the planets inclination. Fourth: the extrapolation of the calculated impact parameter. Fifth: the extrapolation of the calculated transit duration.

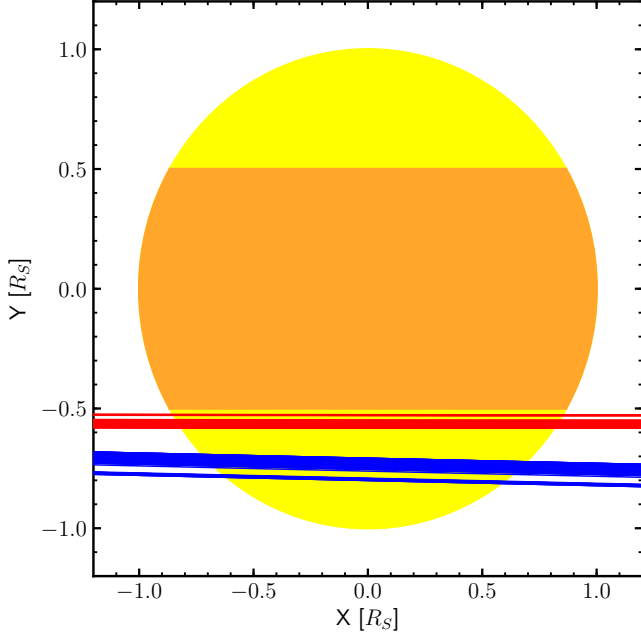


Fig. A.3. The latitude coverage of Kepler-9 (yellow circular disc) by all transit observation of data set III by Kepler-9b (red) and Kepler-9c (blue). Demonstrated is the best model of data set III. The order of the variations can be drawn from Fig.5 or Fig.A.2 respectively, where the fourth row shows the modelled impact parameters. The orange area indicates the possible spot occurrence area between 0° and 30° up- and downwards.

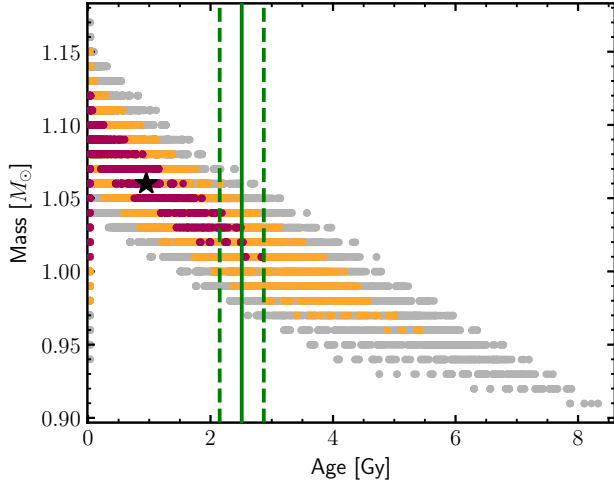


Fig. A.4. Mass-age diagram of Kepler-9 from MESA stellar evolution models (MIST). The black star and the red, orange, and grey dots correspond to the best matching value and the 1σ , 2σ , and 3σ areas derived from results on the density of the data set III photodynamical modeling and from literature values of the effective temperature, the surface gravity, and the metallicity by Holman et al. (2010). The gyrochronological age is indicated by the green solid line and its 1σ range with the green dashed lines.

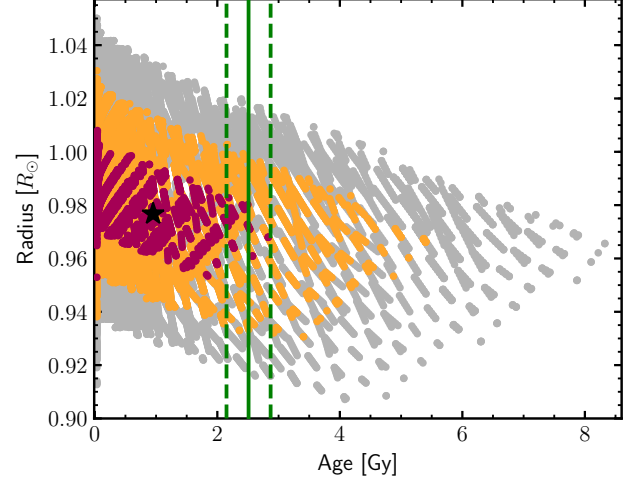


Fig. A.5. Radius-age diagram of Kepler-9 from MESA stellar evolution models (MIST). The black star and the red, orange, and grey dots correspond to the best matching value and the 1σ , 2σ , and 3σ areas derived from results on the density of the data set III photodynamical modeling and from literature values of the effective temperature, the surface gravity, and the metallicity by Holman et al. (2010). The gyrochronological age is indicated by the green solid line and its 1σ range with the green dashed lines.

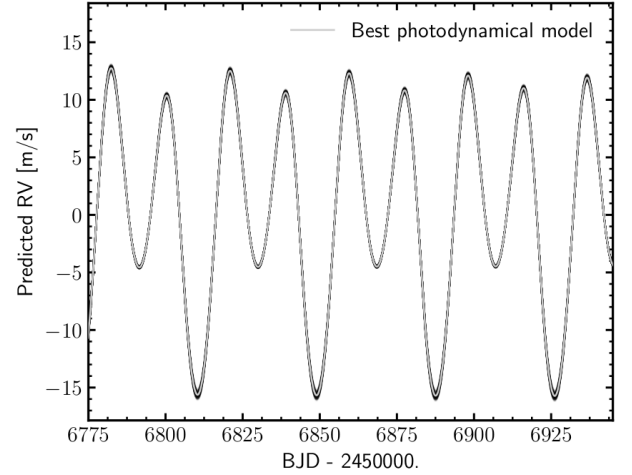


Fig. A.6. Predicted radial velocity measurements from the results of the photodynamical modelling of data set III for the approximate time span of the new observations listed in the HARPS-N archive

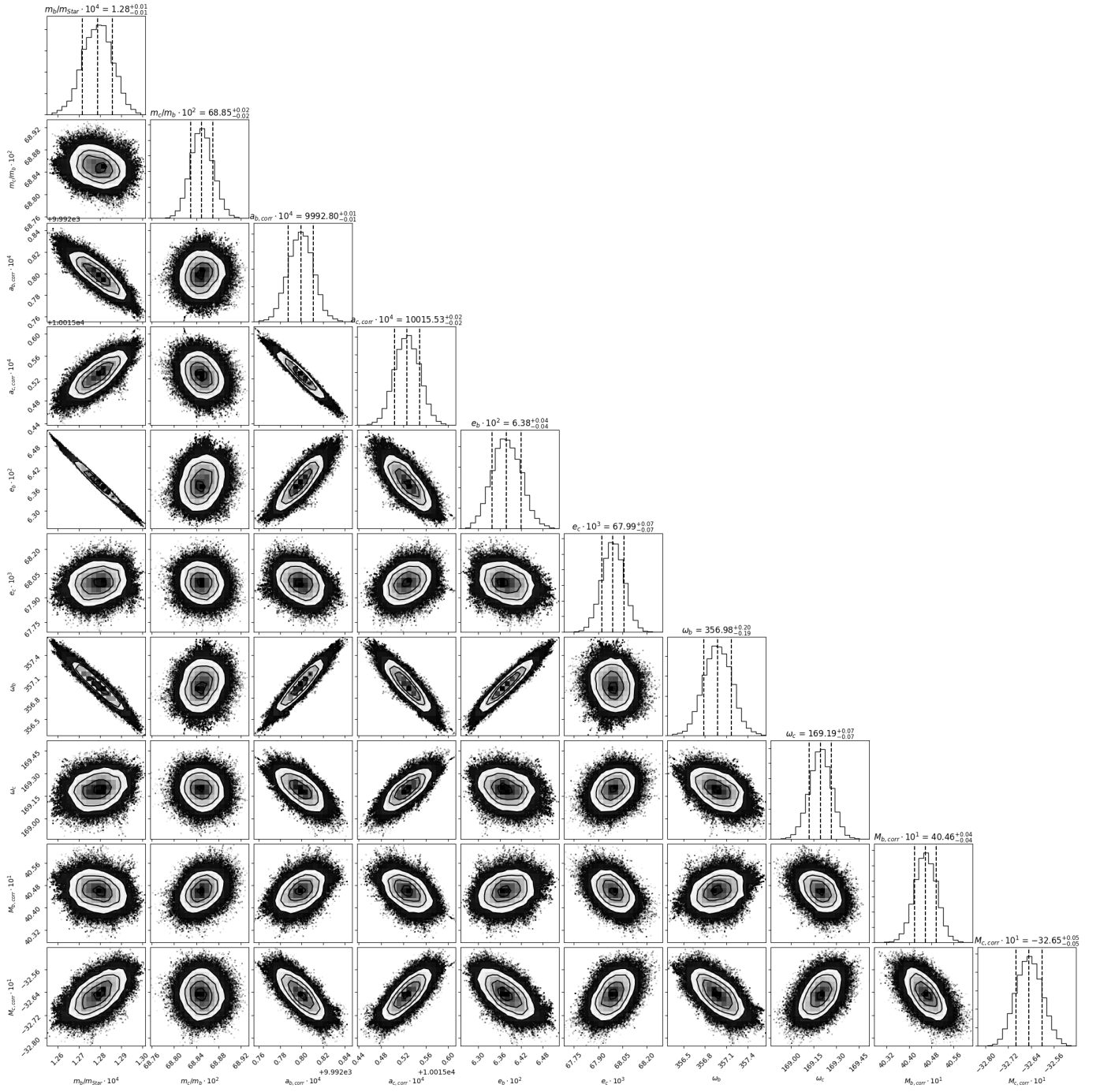


Fig. A.7. Correlation plot of masses, semi-major-axis, eccentricities, longitude of Periastron and mean anomaly from MCMC chains of modelling the full dataset.

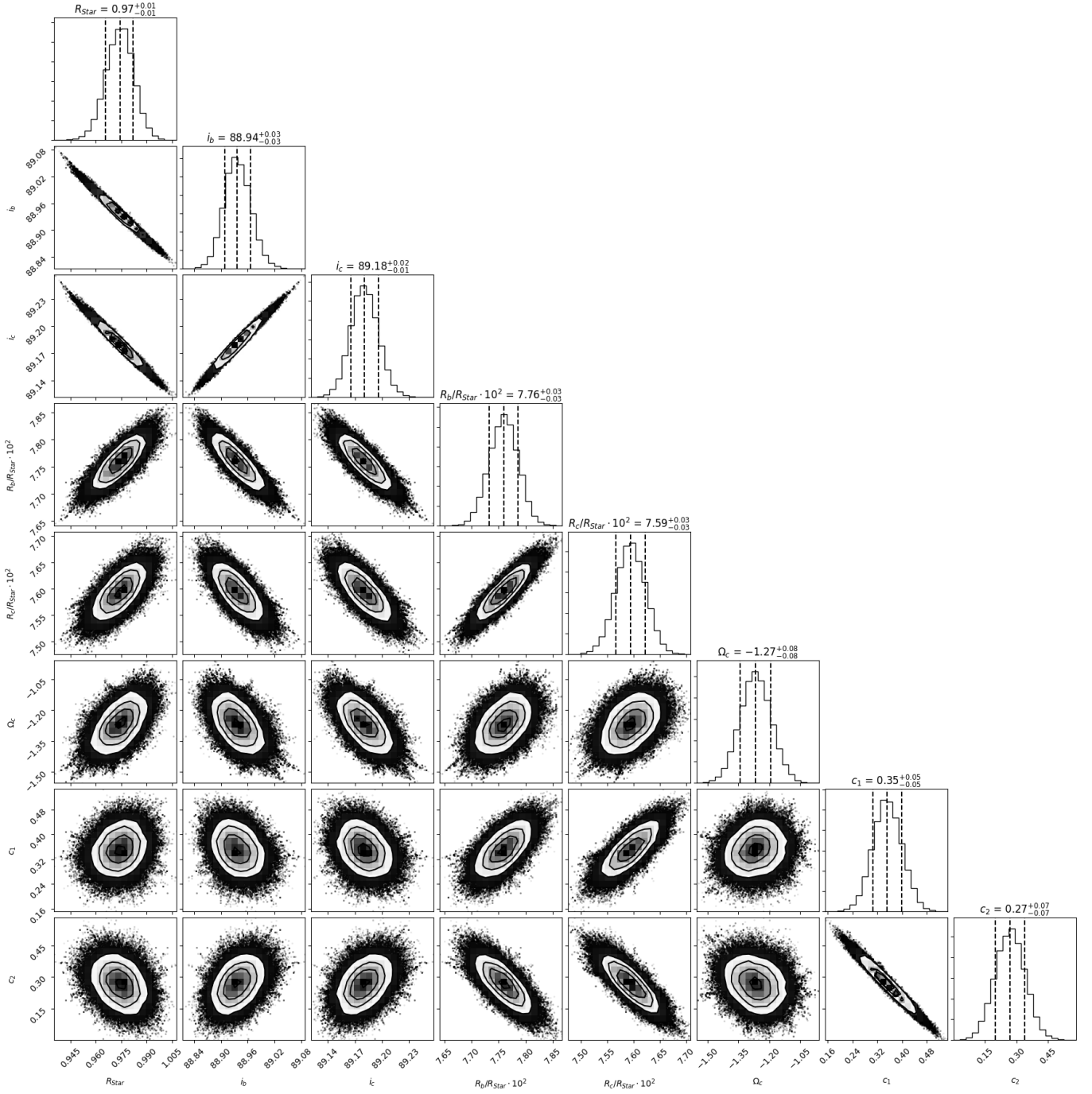


Fig. A.8. Correlation plot of stellar radius, inclination, planetary radii, argument of the ascending node of Kepler-9c and limb darkening coefficients from MCMC chains of modelling the full dataset.

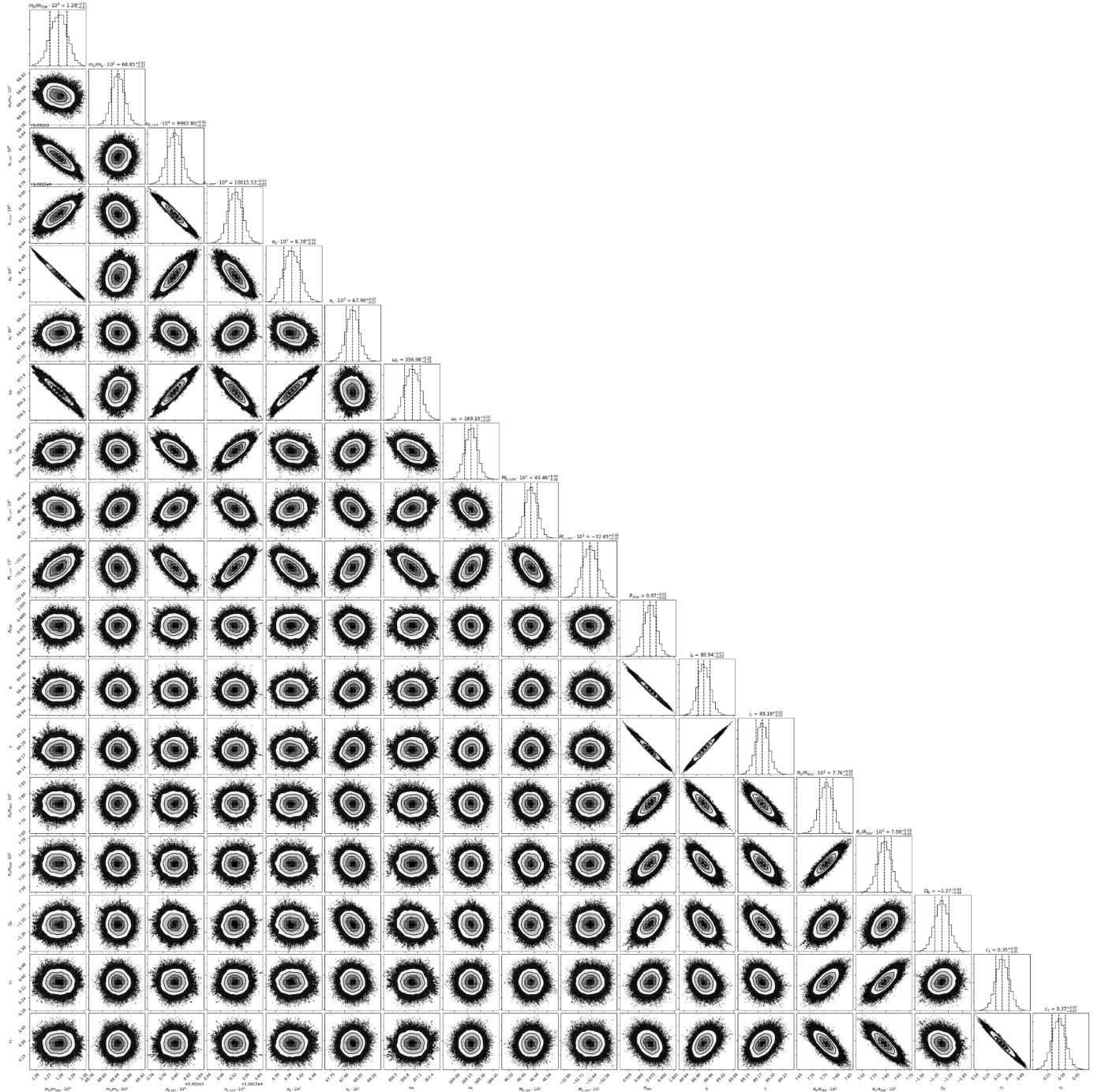


Fig. A.9. Full correlation plot of all fit parameters from modelling the full dataset.

Table A.1. Ephemerides E and transit time predictions in BJD-2400000.0 from modelling data set III for the next 10 years. The median and standard deviation solution of 1000 randomly chosen good models. Reference times for ephemeris E=1: $T_b = 54977.24962(54)$ and $T_c = 54969.30566(78)$

| E | BJD | E | BJD | E | BJD | E | BJD |
|------------|----------------|-----|----------------|-----|----------------|-----|----------------|
| Kepler-9b: | | | | | | | |
| 165 | 58133.0822(7) | 222 | 59230.2853(6) | 279 | 60327.6320(13) | 336 | 61423.9735(30) |
| 166 | 58152.3330(7) | 223 | 59249.5049(6) | 280 | 60346.8684(13) | 337 | 61443.2492(31) |
| 167 | 58171.5797(8) | 224 | 59268.7261(6) | 281 | 60366.0990(12) | 338 | 61462.5362(31) |
| 168 | 58190.8374(9) | 225 | 59287.9463(7) | 282 | 60385.3303(12) | 339 | 61481.8137(31) |
| 169 | 58210.0897(9) | 226 | 59307.1682(7) | 283 | 60404.5561(11) | 340 | 61501.1012(31) |
| 170 | 58229.3543(10) | 227 | 59326.3890(7) | 284 | 60423.7831(11) | 341 | 61520.3792(31) |
| 171 | 58248.6125(10) | 228 | 59345.6117(7) | 285 | 60443.0054(11) | 342 | 61539.6657(31) |
| 172 | 58267.8836(11) | 229 | 59364.8334(7) | 286 | 60462.2291(11) | 343 | 61558.9429(31) |
| 173 | 58287.1474(12) | 230 | 59384.0569(7) | 287 | 60481.4489(10) | 344 | 61578.2269(31) |
| 174 | 58306.4240(12) | 231 | 59403.2799(7) | 288 | 60500.6702(10) | 345 | 61597.5020(30) |
| 175 | 58325.6928(13) | 232 | 59422.5044(7) | 289 | 60519.8885(10) | 346 | 61616.7820(29) |
| 176 | 58344.9740(13) | 233 | 59441.7290(7) | 290 | 60539.1082(10) | 347 | 61636.0537(29) |
| 177 | 58364.2468(13) | 234 | 59460.9550(7) | 291 | 60558.3259(10) | 348 | 61655.3282(28) |
| 178 | 58383.5311(14) | 235 | 59480.1818(7) | 292 | 60577.5447(10) | 349 | 61674.5955(27) |
| 179 | 58402.8069(14) | 236 | 59499.4096(8) | 293 | 60596.7623(10) | 350 | 61693.8635(26) |
| 180 | 58422.0930(14) | 237 | 59518.6395(8) | 294 | 60615.9806(10) | 351 | 61713.1253(25) |
| 181 | 58441.3706(14) | 238 | 59537.8696(8) | 295 | 60635.1985(10) | 352 | 61732.3857(24) |
| 182 | 58460.6569(14) | 239 | 59557.1034(9) | 296 | 60654.4168(10) | 353 | 61751.6414(23) |
| 183 | 58479.9349(14) | 240 | 59576.3366(9) | 297 | 60673.6353(10) | 354 | 61770.8939(22) |
| 184 | 58499.2199(14) | 241 | 59595.5752(10) | 298 | 60692.8538(10) | 355 | 61790.1431(21) |
| 185 | 58518.4971(14) | 242 | 59614.8123(10) | 299 | 60712.0730(10) | 356 | 61809.3878(20) |
| 186 | 58537.7793(14) | 243 | 59634.0566(11) | 300 | 60731.2918(10) | 357 | 61828.6306(20) |
| 187 | 58557.0542(14) | 244 | 59653.2983(11) | 301 | 60750.5118(10) | 358 | 61847.8682(19) |
| 188 | 58576.3322(13) | 245 | 59672.5491(12) | 302 | 60769.7310(10) | 359 | 61867.1050(18) |
| 189 | 58595.6037(13) | 246 | 59691.7960(13) | 303 | 60788.9518(10) | 360 | 61886.3363(17) |
| 190 | 58614.8760(13) | 247 | 59711.0537(14) | 304 | 60808.1716(10) | 361 | 61905.5678(17) |
| 191 | 58634.1429(12) | 248 | 59730.3063(15) | 305 | 60827.3932(10) | 362 | 61924.7941(16) |
| 192 | 58653.4085(12) | 249 | 59749.5708(16) | 306 | 60846.6137(10) | 363 | 61944.0213(16) |
| 193 | 58672.6698(11) | 250 | 59768.8292(17) | 307 | 60865.8362(10) | 364 | 61963.2438(15) |
| 194 | 58691.9279(11) | 251 | 59788.1003(18) | 308 | 60885.0576(10) | 365 | 61982.4676(15) |
| 195 | 58711.1829(10) | 252 | 59807.3642(18) | 309 | 60904.2811(10) | 366 | 62001.6874(15) |
| 196 | 58730.4333(10) | 253 | 59826.6410(19) | 310 | 60923.5038(10) | 367 | 62020.9088(14) |
| 197 | 58749.6817(10) | 254 | 59845.9098(20) | 311 | 60942.7283(10) | 368 | 62040.1269(14) |
| 198 | 58768.9246(9) | 255 | 59865.1912(21) | 312 | 60961.9527(10) | 369 | 62059.3466(14) |
| 199 | 58788.1666(9) | 256 | 59884.4640(21) | 313 | 60981.1787(11) | 370 | 62078.5639(14) |
| 200 | 58807.4026(8) | 257 | 59903.7488(22) | 314 | 61000.4054(11) | 371 | 62097.7826(14) |
| 201 | 58826.6387(8) | 258 | 59923.0246(22) | 315 | 61019.6333(11) | 372 | 62116.9998(14) |
| 202 | 58845.8688(8) | 259 | 59942.3112(22) | 316 | 61038.8630(12) | 373 | 62136.2179(14) |
| 203 | 58865.0999(7) | 260 | 59961.5887(22) | 317 | 61058.0934(12) | 374 | 62155.4354(13) |
| 204 | 58884.3254(7) | 261 | 59980.8757(23) | 318 | 61077.3270(13) | 375 | 62174.6533(13) |
| 205 | 58903.5523(7) | 262 | 60000.1537(22) | 319 | 61096.5605(13) | 376 | 62193.8714(13) |
| 206 | 58922.7744(7) | 263 | 60019.4395(22) | 320 | 61115.7989(14) | 377 | 62213.0895(13) |
| 207 | 58941.9981(7) | 264 | 60038.7167(22) | 321 | 61135.0363(15) | 378 | 62232.3083(13) |
| 208 | 58961.2179(7) | 265 | 60057.9998(22) | 322 | 61154.2805(16) | 379 | 62251.5267(13) |
| 209 | 58980.4393(7) | 266 | 60077.2749(21) | 323 | 61173.5225(17) | 380 | 62270.7463(13) |
| 210 | 58999.6578(7) | 267 | 60096.5539(21) | 324 | 61192.7730(18) | 381 | 62289.9651(13) |
| 211 | 59018.8777(7) | 268 | 60115.8255(21) | 325 | 61212.0202(19) | 382 | 62309.1856(13) |
| 212 | 59038.0957(7) | 269 | 60135.0989(20) | 326 | 61231.2777(20) | 383 | 62328.4050(13) |
| 213 | 59057.3147(7) | 270 | 60154.3660(19) | 327 | 61250.5305(21) | 384 | 62347.6263(13) |
| 214 | 59076.5327(7) | 271 | 60173.6328(19) | 328 | 61269.7949(23) | 385 | 62366.8465(13) |
| 215 | 59095.7514(7) | 272 | 60192.8943(18) | 329 | 61289.0534(24) | 386 | 62386.0687(13) |
| 216 | 59114.9697(7) | 273 | 60212.1536(17) | 330 | 61308.3245(25) | 387 | 62405.2899(13) |
| 217 | 59134.1883(7) | 274 | 60231.4089(17) | 331 | 61327.5884(26) | 388 | 62424.5131(14) |
| 218 | 59153.4073(6) | 275 | 60250.6603(16) | 332 | 61346.8653(27) | 389 | 62443.7355(14) |
| 219 | 59172.6261(6) | 276 | 60269.9091(15) | 333 | 61366.1340(28) | 390 | 62462.9601(14) |
| 220 | 59191.8458(6) | 277 | 60289.1529(14) | 334 | 61385.4156(29) | 391 | 62482.1842(14) |
| 221 | 59211.0649(6) | 278 | 60308.3953(14) | 335 | 61404.6884(30) | 392 | 62501.4102(15) |

| E | BJD | E | BJD | E | BJD | E | BJD |
|------------|----------------|-----|----------------|-----|----------------|-----|----------------|
| Kepler-9c: | | | | | | | |
| 82 | 58125.7907(10) | 111 | 59255.0764(17) | 140 | 60384.0857(19) | 169 | 61514.8518(47) |
| 83 | 58164.7408(11) | 112 | 59294.1486(17) | 141 | 60423.1271(20) | 170 | 61553.6402(46) |
| 84 | 58203.6605(12) | 113 | 59333.2194(17) | 142 | 60462.1834(21) | 171 | 61592.4390(44) |
| 85 | 58242.5493(14) | 114 | 59372.2879(17) | 143 | 60501.2500(22) | 172 | 61631.2545(41) |
| 86 | 58281.4089(16) | 115 | 59411.3529(17) | 144 | 60540.3229(23) | 173 | 61670.0929(38) |
| 87 | 58320.2428(18) | 116 | 59450.4124(17) | 145 | 60579.3991(24) | 174 | 61708.9592(34) |
| 88 | 58359.0557(20) | 117 | 59489.4635(17) | 146 | 60618.4764(25) | 175 | 61747.8572(30) |
| 89 | 58397.8536(21) | 118 | 59528.5028(16) | 147 | 60657.5537(25) | 176 | 61786.7885(27) |
| 90 | 58436.6427(22) | 119 | 59567.5263(16) | 148 | 60696.6301(25) | 177 | 61825.7525(25) |
| 91 | 58475.4297(22) | 120 | 59606.5294(15) | 149 | 60735.7055(25) | 178 | 61864.7467(24) |
| 92 | 58514.2212(21) | 121 | 59645.5080(16) | 150 | 60774.7795(25) | 179 | 61903.7666(25) |
| 93 | 58553.0240(20) | 122 | 59684.4584(17) | 151 | 60813.8522(25) | 180 | 61942.8073(26) |
| 94 | 58591.8444(18) | 123 | 59723.3785(20) | 152 | 60852.9232(24) | 181 | 61981.8635(28) |
| 95 | 58630.6884(17) | 124 | 59762.2678(23) | 153 | 60891.9918(24) | 182 | 62020.9307(29) |
| 96 | 58669.5608(15) | 125 | 59801.1279(26) | 154 | 60931.0567(24) | 183 | 62060.0046(30) |
| 97 | 58708.4650(13) | 126 | 59839.9620(29) | 155 | 60970.1159(23) | 184 | 62099.0820(31) |
| 98 | 58747.4020(12) | 127 | 59878.7749(32) | 156 | 61009.1667(23) | 185 | 62138.1607(32) |
| 99 | 58786.3710(12) | 128 | 59917.5724(33) | 157 | 61048.2058(22) | 186 | 62177.2393(32) |
| 100 | 58825.3689(12) | 129 | 59956.3608(34) | 158 | 61087.2292(21) | 187 | 62216.3170(32) |
| 101 | 58864.3913(13) | 130 | 59995.1465(34) | 159 | 61126.2324(21) | 188 | 62255.3933(32) |
| 102 | 58903.4329(14) | 131 | 60033.9364(33) | 160 | 61165.2112(22) | 189 | 62294.4682(32) |
| 103 | 58942.4889(15) | 132 | 60072.7371(32) | 161 | 61204.1622(24) | 190 | 62333.5415(32) |
| 104 | 58981.5547(16) | 133 | 60111.5551(29) | 162 | 61243.0830(28) | 191 | 62372.6128(32) |
| 105 | 59020.6264(16) | 134 | 60150.3963(27) | 163 | 61281.9731(32) | 192 | 62411.6815(31) |
| 106 | 59059.7012(17) | 135 | 60189.2658(24) | 164 | 61320.8338(37) | 193 | 62450.7463(30) |
| 107 | 59098.7772(17) | 136 | 60228.1670(21) | 165 | 61359.6686(41) | 194 | 62489.8054(30) |
| 108 | 59137.8532(17) | 137 | 60267.1014(19) | 166 | 61398.4818(44) | | |
| 109 | 59176.9285(17) | 138 | 60306.0681(18) | 167 | 61437.2792(46) | | |
| 110 | 59216.0030(17) | 139 | 60345.0643(18) | 168 | 61476.0670(47) | | |